Nuclear organisation and replication timing are coupled through RIF1-PP1 interaction

Stefano Gnan [1,2,3], Ilya M. Flyamer [4,$], Kyle N. Klein [5,$], Eleonora Castelli [2,6], Alexander Rapp [7], Andreas Maiser [8], Naiming Chen [2], Patrick Weber [7], Elin Enervald [1,2], M. Cristina Cardoso [7], Wendy A. Bickmore [4], David M. Gilbert [5] and Sara C. B. Buonomo [1,2,*]

1 Epigenetics & Neurobiology Unit, European Molecular Biology Laboratory (EMBL Rome), Monterotondo, Italy.
2 Institute of Cell Biology, School of Biological Sciences University of Edinburgh, Roger Land, Building, Alexander Crum Brown Road, Edinburgh, EH9 3FF, UK.
3 Current address: Institute Curie, CNRS UMR3244, Pavillon Trouillet-Rossignol, 26 Rue d'Ulm, 75005 Paris, France.
4 MRC Human Genetics Unit, Institute of Genetics and Molecular Medicine, University of Edinburgh, Crewe Road South, Edinburgh EH4 2XU, UK.
5 Department of Biological Science, Florida State University, Tallahassee, Florida 32306, USA.
6 Current address: Friedrich Miescher Institute for Biomedical Research, 4058 Basel, Switzerland.
7 Cell Biology and Epigenetics, Department of Biology, Technical University of Darmstadt, 64287 Darmstadt, Germany.
8 Department of Biology II, LMU Munich, 81377 Munich, Germany.

[$]These authors contributed equally to the work
[*]Corresponding author and lead contact: sara.buonomo@ed.ac.uk

Keywords: replication timing, nuclear organisation, Rif1, replication foci, PP1

Abstract
Three-dimensional genome organisation and replication timing are known to be correlated, however, it remains unknown whether nuclear architecture overall plays an instructive role in the replication-timing program and, if so, how. Here we demonstrate that RIF1 is a molecular hub that co-regulates both processes. Both nuclear organisation and replication timing depend upon the interaction between RIF1 and PP1. However, whereas nuclear architecture requires the full complement of RIF1 and its interaction with PP1, replication timing is not sensitive to RIF1 dosage. RIF1's role in replication timing also extends beyond its interaction with PP1. Availing of this separation-of-function approach, we have therefore identified in RIF1 dual function the molecular bases of the co-dependency of the replication-timing program and nuclear architecture.

Introduction

In eukaryotes, origins of DNA replication are not activated all at once. Origin firing follows a cell-type specific temporal program known as DNA replication timing. The replication-timing program is mirrored by the spatial distribution in the nucleus of replication foci, which are clusters of about 5 simultaneously activated bidirectional replication forks (Chagin et al., 2016). Both spatial and temporal replication patterns are re-established every cell cycle in G1, at the timing decision point (TDP) (Dimitrova and Gilbert, 1999), that coincides with chromosomal territories achieving their stable, reciprocal position (Muller et al., 2010) and the re-establishment of chromatin architecture and interphase-nuclear configuration (Dileep et al., 2015; Nagano et al., 2017). The spatial organisation of DNA replication is evident at multiple levels. The units of DNA replication timing, replication domains (RD), coincide with one of the basic units of three-dimensional (3D) genome organisation, the topologically associated domains (TADs) (Pope et al., 2014). Recently, *in cis* elements (early replicating control elements-ERCEs) that can simultaneously influence chromatin looping and replication timing have also been identified (Sima et al., 2019). Moreover, the "assignment" of RDs as early or late replicating (the establishment of the replication-timing program), takes place on a chromosome-domain level, prior to the specification of the active origins of replication (Dimitrova and Gilbert, 1999). On a global scale, the early and late replicating genomes overlap with the A and B compartments identified by Chromosome Conformation Capture methods (HiC) (Moindrot et al., 2012; Ryba et al., 2010; Yaffe et al., 2010) and are segregated in the nuclear interior or the periphery of the nucleus and nucleolus respectively. Finally, a recent study from budding yeast has shown that activation of early origins drives their internalisation (Zhang et al., 2019). However, no causal link between the temporal and spatial aspects of DNA replication organisation has been established.

RIF1 is a key genome-wide regulator of replication timing (Cornacchia et al., 2012; Foti et al., 2016; Hayano et al., 2012; Hiraga et al., 2014; Peace et al., 2014; Seller and O'Farrell, 2018; Yamazaki et al., 2012). It is also involved in re-establishing spatial chromatin organisation in the nucleus at G1 (Foti et al., 2016), and in the control of replication foci spatial dynamics (Cornacchia et al., 2012). RIF1 could therefore be a molecular connection between the temporal and spatial organisation of DNA replication in mammalian cells.

The molecular function of RIF1 is still unclear, although it is involved in a variety of functions such as DNA repair (Buonomo et al., 2009; Chapman et al., 2013; Daley and Sung, 2013; Di Virgilio et al., 2013; Feng et al., 2013; Gupta et al., 2018; Hengeveld et al., 2015; Martina et al., 2014; Mirman et al., 2018; Noordermeer et al., 2018; Silverman et al., 2004; Spies et al., 2019), telomere length regulation in yeast (Gallardo et al., 2011; Hardy et al., 1992; Mattarocci et al., 2017; Shi et al., 2013; Teixeira et al., 2004), cytokinesis (Bhowmick et al., 2019), epigenetic (Daxinger et al., 2013; Li et al., 2017; Tanaka et al., 2016; Toteva et al., 2017; Zofall et al., 2016) and DNA replication-timing control. Mammalian RIF1 (266 kDa) interacts with components of the nuclear lamina (Foti et al., 2016; Roux et al., 2012), behaving as an integral part of this insoluble nuclear scaffold and chromatin organiser. RIF1 associates with the late replicating genome, forming megabase-long domains called RIF1-associated-domains (RADs) (Foti et al., 2016). It is unknown what directs the association to chromatin, but both the N and C terminus of RIF1 have been shown to be capable of mediating interaction with DNA (Kanoh et al., 2015; Mattarocci et al., 2017; Moriyama et al., 2017; Moriyama et al., 2018; Sukackaite et al., 2014; Xu et al., 2010). RIF1 has a highly-conserved interaction with Protein Phosphatase 1 (PP1) that is reported to be critical to regulate the firing of individual, late origins of replication (Alver et al., 2017; Dave et al., 2014; Hiraga et al., 2014; Hiraga et al., 2017; Mattarocci et al., 2014). Activation of these origins is promoted by RIF1 removal in late S-phase, led by the increasing levels of cyclin-dependent Kinase (CDK) activity (Alver et al., 2017; Dave et al., 2014; Hiraga et al., 2014; Hiraga et al., 2017; Mattarocci et al., 2014; Seller and O'Farrell, 2018).

These studies therefore place the role of the RIF1-PP1 interaction at the stage of execution of the replication-timing program, in S-phase. However, we have also identified a role for RIF1 as a chromatin organiser earlier during the cell cycle, in G1, around the time of the establishment of the replication-timing program (Foti et al., 2016). Rif1 deficiency impacts nuclear architecture, relaxing the constraints that normally limit chromatin interactions between domains with the same replication timing (Foti et al., 2016). It is unknown if Rif1-dependent chromatin architecture establishment affects the replication-timing program, how RIF1 contributes to nuclear organisation, and if and how the interaction with PP1 plays a role in this function. More generally, the functional relationship between nuclear architecture and replication timing is still unclear.

Here, we tackle this question by interfering with the RIF1-PP1 interaction, introducing point mutations in RIF1 that specifically abolish the interaction. Our results show that both replication timing and nuclear organisation depend upon RIF1-PP1 interaction. However, unlike the replication-timing program, we find that nuclear organisation is exquisitely sensitive to RIF1's dosage. Using this separation-of-function approach, we identify in RIF1 the molecular hub for their co-regulation. In addition, we show for the first time that the replication-timing program can be established and executed independent of the three-dimensional (3D) organisation or the spatial distribution of replication foci.

Results

Mouse embryonic stem cells expressing *Rif1$^{\Delta PP1}$*

RIF1-PP1 interaction promotes the continuous dephosphorylation of MCM4 at replication origins that are "marked" to be activated only during the later part of S-phase (Alver et al., 2017; Dave et al., 2014; Hiraga et al., 2014; Hiraga et al., 2017; Mattarocci et al., 2014). This suggests that, through RIF1, PP1 contributes to the control of the timing of firing of individual origins of replication. However, the functional significance of RIF1-PP1 interaction for the establishment and domain-level regulation of the replication-timing program, and in the context of nuclear 3D organisation is unknown.

Mutations that perturb RIF1-PP1 interaction are potential tools to achieve separation-of-function between nuclear organisation and replication timing. We have recently identified the sites within RIF1 that mediate the physical contacts with PP1 (SILK and RVSF motifs, residues 2128–2131 and 2150–2153). Point mutations of these residues reduce PP1 interaction to undetectable levels (RIF1$^{\Delta PP1}$: SILK into SAAA and RVSF into RVSA, (Sukackaite et al., 2017)). We therefore sought to express the *Rif1$^{\Delta PP1}$* mutant in mESCs. However, *Rif1* overexpression is toxic and therefore, in order to create a system to expresses *Rif1$^{\Delta PP1}$* in a physiological context, we have utilised *Rif1$^{FH/flox}$* mESCs. In these cells, one allele of *Rif1* contains loxP sites flanking exons 5 to 7 ((Buonomo et al., 2009), *Rif1^{flox}*)), while the second is a knock-in of a FLAG-HA2 tag (FH) into the *Rif1* locus (*Rif1^{FH}*) ((Cornacchia et al., 2012), Fig. S1A and B)). We then targeted the FH allele with a mini-gene encoding *Rif1$^{\Delta PP1}$*. As a control, following the same strategy, we have also knocked-in a *Rif1* wild type mini-gene (*Rif1^{TgWT})*. Thus, Cre-mediated deletion of the *Rif1^{flox}* allele leaves either the FH-tagged *Rif1$^{\Delta PP1}$*, *Rif1^{TgWT}* or the parental *Rif1^{FH}* allele as the sole source of RIF1, effectively creating inducible FH-tagged *Rif1* hemizygous cells. Upon tamoxifen-mediated Cre recombination, we have then studied the consequences of abolishing RIF1-PP1 interaction in *Rif1$^{\Delta PP1/flox}$* (*Rif1$^{\Delta PP1/-}$*, abbreviated Rif1-ΔPP1), control *Rif1$^{TgWT/flox}$* (*Rif1$^{TgWT/-}$* abbreviated Rif1-TgWT) and the parental cell line *Rif1$^{FH/flox}$* (*Rif1$^{FH/-}$*, abbreviated Rif1-FH) cell lines. In agreement with the fact that, upon Cre induction, all the Rif1 FH-tagged alleles are hemizygous, RIF1-ΔPP1, RIF1-TgWT and RIF1-FH, are expressed at

comparable levels (Fig. 1A, B and S1C) and RIF1-PP1 interaction is undetectable in RIF1-ΔPP1 (Fig. 1C). Both RIF1-ΔPP1 and RIF1-TgWT have a comparable degree of chromatin-association (Fig. 1D).
RIF1 deficiency in mESCs affects nuclear function at multiple levels. One of the features of Rif1-KO cells is the doubling of the population in G2, accompanied by a decreased S-phase population (Fig. 1E and (Foti et al., 2016)). Our data show that *Rif1* hemizygosity (*Rif1-FH* and *Rif1-TgWT*) results in an altered cell cycle similar to RIF1 deficiency (Fig. 1E). Importantly, cell cycle-distribution in both *Rif1-ΔPP1* and *Rif1-TgWT* cell lines appears comparable to *Rif1-FH* cells. These results suggest that the defective cell cycle progression of *Rif1* null cells is not attributable to altered PP1 function but to insufficient levels of RIF1.
Loss of Rif1 function also results in the alteration of the gene expression profile in mESCs (Foti et al., 2016), including the de-repression of MERVLs (Li et al., 2017), an effect that RIF1 shares with other epigenetic and DNA replication regulators (Yang et al., 2015). We therefore compared the level of MERVL RNA in *Rif1-WT*, *Rif1-KO*, *Rif1-TgWT* and *Rif1-ΔPP1* cells. After four days of deletion, MERVLs are upregulated not only in *Rif1-ΔPP1* and *Rif1-KO* cells, but, surprisingly, also in the hemizygous controls (Fig. 1F), suggesting that, as for cell cycle progression, gene expression control is also sensitive to RIF1 dosage.

RIF1-PP1 interaction is important for the replication-timing program

The most conserved function of RIF1 is the control of the replication-timing program and *Rif1-KO* cells show pronounced genome-wide changes in the temporal program of origin firing (Cornacchia et al., 2012; Foti et al., 2016). As RIF1-PP1 interaction has been shown to be important, at least during the execution of the replication-timing program in S-phase, (Alver et al., 2017; Dave et al., 2014; Hiraga et al., 2014; Hiraga et al., 2017; Mattarocci et al., 2014), expression of $Rif1^{\Delta PP1}$ should affect replication timing to a similar extent to *Rif1* deletion. In agreement with this prediction, hierarchical clustering of genome-wide replication timing shows that *Rif1-ΔPP1* and *Rif1-KO* mESCs cluster together, while $Rif1^{+/+}$ (*Rif1-WT*) and control hemizygous (*Rif1-FH* and *Rif1-TgWT*) cells form a separate cluster (Fig. 2A and S2A). The replication profiles of both *Rif1-ΔPP1* and *Rif1-KO* mESCs appear similarly compressed around the zero (Fig. 2B and S2B), and a comparable fraction of the genome displays replication timing switches and changes (Fig. S3), suggesting an analogous loss of temporal control of origin firing in both cases. Importantly, the replication timing changes induced by the expression of $Rif1^{\Delta PP1}$ are not attributable to *Rif1* haploinsufficiency. In fact, the replication-timing profiles of *Rif1* hemizygous controls (*Rif1-FH* and *Rif1-TgWT*), are very similar to the wild type cells (*Rif1-WT*, Fig. 2B and C). Despite the similarities, however, the impact of loss of RIF1 versus loss of RIF1-PP1 interaction on the replication-timing program is not identical. $Rif1^{\Delta PP1}$ expressing cells maintain a better degree of distinction between earlier and later replicating domains than *Rif-KO* (Fig. 2B, C and Fig. S2B). These data suggest that RIF1-dependent control of the replication-timing program is not entirely exerted through PP1 and some other function of RIF1 partially contributes as well.

DNA replication timing is independent of the spatial distribution of replication foci

DNA replication takes place in a spatially organised manner (Nakamura et al., 1986; Nakayasu and Berezney, 1989), with the distribution of replication foci correlated to the time of replication (Fox et al., 1991). We have shown that in mouse primary embryonic fibroblasts (pMEFs), RIF1 deficiency induces changes of both the spatial distribution of replication foci and replication timing (Cornacchia et al., 2012). We find a comparable effect in RIF1 deficient mESCs, with an increase of cells displaying an early-like replication pattern (Fig. 2D) despite there being no increase in the proportion of cells in early S-phase, as judged from the analysis of DNA content (Fig. S2C). In wild type cells, during early S-phase (defined as diffuse nucleoplasmic EdU and MCM3 staining and absence of histone H3

phosphorylated on Ser10-H3S10p), the replication pattern features many small replication foci throughout the nucleoplasm (Fig. S4A). In *Rif1-KO* cells, a similar distribution of replication foci (EdU) also appears aberrantly in cells in later S-phase (clusters of H3S10p signal, often at chromocenters, MCM3 discrete foci, larger-mid- or smaller-late and peripheral) (Fig. S4B). Normally at this stage, EdU signal appears as discrete foci of different sizes (Fig. S4A).
To study the effect of *Rif1* deficiency or expression of *Rif1*$^{\Delta PP1}$ on the total number of replication forks and their clustering, we have employed 3D-structure illumination microscopy (SIM-Fig. S5A). Since *Rif1* deletion and expression of *Rif1*$^{\Delta PP1}$ induce a loss of equivalence between replication foci distribution and replication timing, we could not analyse early, mid and late S-phase separately. *Rif1* deficiency results in an increase of the total number of replication forks (Fig. S5B) that could explain the apparent increase in the proportion of cells displaying early-like replication patterns. However, expression of *Rif1*$^{\Delta PP1}$ does not alter the total number of replication forks per nucleus (Fig. S5B), yet it causes an accumulation of early-like replication patterns that is comparable to *Rif1-KO* cells (Fig. 2D). Considering the different extent of the impact of loss of RIF1 (*Rif1-KO)* and loss of RIF1-PP1 interaction (*Rif1-ΔPP1*) on replication timing, this discrepancy in the effect on the total number of forks is interesting and indicates that the altered distribution of replication foci observed in both cell lines is not linked to the change of total number of replication forks. Moreover, by matching the total number of replication forks to the number of replication foci, we could not find a correlation between the number of forks per replication focus (Fig. S5C) and the changes of distribution of replication patterns (Fig. 2D). These data indicate that the increase of the proportion of cells with early-like replication patterns observed in *Rif1-KO* and *Rif1-ΔPP1* cells is not attributable to the de-clustering of the replication forks. Finally, our analysis shows that Rif1 hemizygosity (Rif1-hem=*Rif-FH+Rif1-TgWT*) has an impact on the spatial distribution of replication foci that is similar to, although milder, than *Rif1* deficiency or expression of *Rif1*$^{\Delta PP1}$ (Fig. 2D). However, hemizygosity does not result in an increased number of total replication forks or a measurable perturbation of the replication-timing program. These results suggest that spatial distribution of replication foci and the timing of replication can be uncoupled. In conclusion, loss or reduced RIF1 levels and loss of RIF1-PP1 interaction all impact on the distribution of replication foci, but not all affect replication timing.

RIF1 dosage is important for nuclear compartmentalisation

The distribution of replication foci in the nucleus reflects the spatial organisation of the underlying chromatin. As a consequence, the altered spatial configuration of replication foci in *Rif1-hem* and *Rif1-ΔPP1* cells suggests that a reduced amount of RIF1 or loss of RIF1-PP1 interaction could affect chromatin organisation similarly to what we have shown for *Rif1* null cells (Foti et al., 2016), and irrespective of their effects on replication timing. We therefore analysed 3D chromatin organisation in *Rif1-KO*, *Rif1-ΔPP1* and *Rif1-hem* cells by Hi-C. We have previously shown by 4C that *Rif1* deficiency induces an increase of low-frequency contacts between TADs with different replication timing (Foti et al., 2016). In agreement with this, our Hi-C data indicate that *Rif1* deletion increases chromatin contacts *in cis,* especially at long range (>10Mbp) (Rif1-WT and Rif1-KO, Fig. 3A and B). The contacts gained preferentially involve late-replicating genomic regions associating with early-replicating regions (Fig. 4A) and RIF1-enriched regions gaining contacts with RIF1-poor genomic regions (Fig. 4B). These changes cannot be explained by the increased fraction of cells in G2 in Rif1-KO and Rif1-ΔPP1 cells, as it was shown that chromosome compaction in G2/M favours the establishment of short-range interactions (Nagano et al., 2017). They suggest instead the alteration of the A/B compartmentalisation in mutant cells compared with *Rif1-WT* cells. Indeed, principle component analysis shows that *Rif1-WT* and *Rif1-KO* display a distinctly different compartment organisation (Fig. 4C). In agreement with previous data that have reported a more “open chromatin” (Cornacchia et al., 2012; Foti et al., 2016; Yamazaki et al., 2012), *Rif1*’s loss of function induces an

expansion of the A compartment (and corresponding contraction of the B compartment, Fig. 4D) and compartment strength is weakened (Fig. 4E and F). Loss of RIF1-PP1 interaction induces alterations of chromatin organisation comparable to Rif1-KO (Fig. 4C), with a similar degree of expansion of the A compartment (Fig. 4D) and weakened compartment definition (Fig. 4E and F). This supports the conclusion that PP1 plays a key role in RIF1-dependent control of chromatin organisation.

Unexpectedly, chromatin architecture in *Rif1* hemizygous cells (Rif1-FH and Rif1-TgWT) shows an intermediate but reproducible degree of change. Halving *Rif1* dosage, is sufficient to induce a gain of *in cis* contacts between distant genomic regions (Fig. 3A) of opposite replication timing (Fig. 4A). Accordingly, principal component analysis (PCA) of the overall A/B compartment organisation in Rif1-TgWT and Rif1-FH cells lies between with *Rif1* null and Rif1-ΔPP1 cells and RIF1-WT (Fig. 4C), with an expansion of the A compartment (Fig. 4D) and weakened compartmentalisation (Fig. 4E and F) that is intermediate between Rif1-WT and Rif1-KO/Rif1-ΔPP1 cells. These data indicate that chromatin architecture is exquisitely sensitive to RIF1 dosage, and that decreasing the levels of RIF1 induces a progressive alteration of nuclear organisation. This is in striking contrast with the effect of varying RIF1 levels on the regulation of replication timing.

Discussion

The remarkable coincidence of spatial distribution and replication timing of different portions of the genome, at multiple levels of organisation and throughout evolution, has encouraged the idea of a causal relationship between nuclear architecture and replication timing. At a molecular level, their covariation - for example during cell fate determination and embryonic development - finds a confirmation in their co-dependence on RIF1. In this work, we show that both aspects of nuclear function depend upon the interaction between RIF1 and PP1. However, 3D organisation of chromatin contacts and replication timing show a different degree of dependency on RIF1-PP1 interaction and are differentially influenced by RIF1's dosage. The loss of RIF1-PP1 interaction affects the compartmentalisation of chromatin contacts comparable to a complete loss of RIF1 function, while it only partially recapitulates the effects of *Rif1*$^{-/-}$ on the control of replication timing. In addition, the former is sensitive to RIF1's dosage, while *Rif1's* haploinsufficiency does not affect the latter.

RIF1 is known to multimerise (Kobayashi et al., 2019; Moriyama et al., 2018; Xu et al., 2010) and to interact with the nuclear lamina (Foti et al., 2016; Roux et al., 2012). RIF1 multimers could act as a sub-stochiometric platform, interacting with different regulators of replication timing, in addition to PP1. In this case, the consequences of the complete loss of RIF1 function on the replication-timing program would amount to the sum of perturbation of multiple pathways that control the timing of origin activation. For example, RIF1-ΔPP1 may only specifically interfere with the PP1-dependent control of DDK (Dbf4-dependent kinases) activity at origins, while other RIF1 interactors may contribute to the epigenetic control of origin activation. The proteins associated with RIF1 are enriched for chromatin and epigenetic regulators (Sukackaite et al., 2017), and the contribution of histone modifiers to the control of replication timing has long been recognised (Jorgensen et al., 2007; Li et al., 2005; Takebayashi et al., 2013; Vogelauer et al., 2002; Yokochi et al., 2009; Yoshida et al., 2014). However, an understanding of the effect of *Rif1* deletion on the epigenetic landscape is still missing, leaving this hypothesis currently hard to test (Cornacchia et al., 2012; Dan et al., 2014; Foti et al., 2016; Li et al., 2017). In the context of chromatin architecture organisation, RIF1 multimers could directly participate in the creation of local scaffolds that restrict chromatin mobility or, alternatively, could regulate other proteins with this role. In either case, a reduction of RIF1 dosage could have structural, quantitative consequences.

Our results identify RIF1 as a molecular link, a point of convergence and co-regulation. We propose that RIF1, specifically, and not generic nuclear architecture, coordinates the replication-timing program with nuclear 3D organisation. In agreement with this view, recent data show that cohesins and CTCF are not involved in the regulation of replication timing (Oldach and Nieduszynski, 2019; Sima et al., 2019) and that the definition of A/B compartments and Early/Late replicating domains is uncoupled at the time of zygotic genome activation in zebrafish (Kaaij et al., 2018). Altogether, these data suggest that replication timing and nuclear architecture, or at least 3D organisation of chromatin contacts and spatial distribution of replication foci, are not linked by a causative relationship. Yet, they are coregulated, both during cell cycle and embryonic development, and RIF1 is a point of convergence. Having established this, is an important step to start addressing the fundamental question of why this coordination is important. During embryonic development in different organisms, for example in *Drosophila melanogaster*, replication timing (Seller and O'Farrell, 2018) and TADs definition both emerge around the time when zygotic transcription starts (Ogiyama et al., 2018). Could uncoupling these two events have consequences on gene expression? We can alter chromatin organisation, leaving replication timing intact, by halving RIF1 dosage. This affects cell cycle progression and the repression of MERVLs (this work). In a complementary approach, it has been shown that alteration of replication timing by overexpression of limiting replication factors during early *Xenopus laevis* development, that presumably leaves nuclear architecture intact, affects the onset of zygotic transcription and the transition into gastrulation (Collart et al., 2013). It is therefore tempting to speculate that the covariation of replication timing and nuclear architecture could be important to coordinate gene expression and the choice of origins of replication.

Acknowledgments

We would like to acknowledge Martin Waterfall from the IIIR Flow Cytometry Core Facility, University of Edinburgh; David Kelly from the COIL facility, WTCCB, University of Edinburgh; Vladimir Benes and the Genomic Core Facility at EMBL Heidelberg; Philip Hublitz from Gene expression Facility, EMBL Monterotondo; Violetta Parimbeni for mouse husbandry, EMBL Monterotondo. SG was funded by ERC consolidator award 726130 to SCBB; EC was supported by the Erasmus Program. EE received funding from the European Union's Horizon 2020 research and the Marie Skłodowska-Curie Individual Fellowship grant agreement No. 660985 and from the ERC consolidator award 726130 to SCBB. IMF was funded by the Darwin Trust of Edinburgh. SCBB thanks the ERC, DMG thanks NIH grant GM083337, WAB is funded by a Medical Research Council University Unit programme grant [MC_ UU_00007/2]. MCC was funded by the Deutsche Forschungsgemeinschaft (DFG, German Research Foundation) – Project-ID 393547839 – SFB 1361 TP06 and DFG grant CA 198/9-2.

Author Contributions

SG has created the cellular system, performed the majority of the experiments and the bioinformatics analysis. IMF has helped with HiC experiments and analysis. KNK has performed the replication timing measures. EC and NC have stained and scored with SG replication-timing patterns. PW, AR and AM have respectively stained cells, acquired 3D-SIM images and performed the analysis. EE has analysed MERVL expression. WAB, DMG, MCC have supported the work with personnel,

resources, scientific discussions and critical reading of the manuscript. SCBB has conceived the project, performed some of the experiments and written the manuscript.

Declaration of Interests

The authors declare no competing interests.

Figure Legends

Figure 1. **Expression levels and chromatin association of RIF1-TgWT and RIF1-ΔPP1 are comparable to those of *Rif1* hemizygous cells.**

A. Quantitative analysis of total levels of FH-tagged RIF1, measured by intra-cellular FACS staining. Anti-HA mouse ascites 16B12 was used to stain the indicated cell lines. *Rif1*$^{FH/FH}$= homozygous knock-in FH-tagged RIF1, as a control of quantitative staining. The plot shows distributions of densities from HA signal, measured in arbitrary units. One representative experiment is shown.
B. Quantification from Fig. 1A. The bar plot represents the median intensities for the experiment shown and the error bars indicate 95% confidence intervals.
C. Total proteins were extracted from cells expressing either untagged, wild type RIF1 (WT), hemizygote RIF1-TgWT or RIF1-ΔPP1 (HA tagged), and immunoprecipitated with anti-HA antibody. The input, immunoprecipitated complex and flow through were analysed by western blot with anti-mouse RIF1 affinity-purified rabbit polyclonal antibody (1240) and anti-PP1α.
D. Quantitative analysis of the levels of chromatin-associated FH-tagged RIF1 throughout the cell cycle (one representative experiment), measured by FACS staining. Cytoplasmic and nucleoplasmic proteins were pre-extracted before fixing chromatin-associated proteins. Anti-HA mouse ascites 16B12 was used to visualize FH-tagged RIF1 as in A. Cell cycle stage was determined by DNA quantification (DAPI staining).
E. Cell cycle distribution of the indicated cell lines, as determined by FACS quantification of EdU incorporation (S-phase) and DAPI staining (DNA amount). The average value of three independent clones per genotype is shown. Average of three experiments. Error bars indicate the standard deviation. *P* values are calculated using Wilcoxon test.
F. Quantification by qRT-PCR of MERVL's upregulation in the indicated genotypes, expressed as fold increase over MERVL levels in the same cell lines, before Cre induction. GAPDH was used to normalize. One representative experiment is shown and displays the average of 3 biological replicates for *Rif1-ΔPP1* and *Rif1-TgWT*, 2 for *Rif1-KO* and one reference for *Rif1-WT*. Error bars indicate standard deviations.

Figure 2. **Effect of loss of RIF1-PP1 interaction on the replication-timing program and on the spatial distribution of replication foci.**

A. Hierarchical cluster analysis of Pearson correlation coefficient of genome-wide replication-timing (RT) profiles between replicas, bin size 50kb. The analysis shows preferential clustering of RT distribution from Rif1-KO and Rif1-ΔPP1 lines, while RT distribution from Rif1-WT clusters with Rif1-TgWT and Rif1-FH lines.
B. Representative RT profile from Chromosome 17. The solid line shows the average of three biological replicas, except for Rif1-FH (single, parental clone). RT scores are calculated as the $\log_2$ of the ratio between mapped reads in the early and late replicating fractions of the cell cycle over bins of 50Kb.
C. Genome-wide distribution of 50kb genomic windows on the bases of their RT scores. Average of three independent lines per genotype is shown, except for Rif1-FH. Shaded areas represents standard deviations. RT scores from Rif1-WT and Rif1 hemizygous lines (Rif1-TgWT and Rif1-FH) show a bimodal distribution, defining distinct early and late genomic regions. On the contrary, the distribution of RT scores from Rif1-KO lines shows a tendency towards a unimodal distribution, centered around zero. Rif1-ΔPP1 lines display an increase of the windows with RT=0, but still a bimodal distribution of the RT values.
D. The spatial distribution of replication foci (replication patterns) was visualized by EdU and DAPI staining. Cells were pulsed for 30 minutes with EdU and fixed. Examples in Fig. S3A. Pie charts show the relative distribution of S-phase cells (EdU positive) between replication patterns corresponding to early, mid and late S-phase. For each genotype, three independent lines and two separate experiments were blind-scored. As Rif-FH cells are a single cell line with no biological replicas (parental) and the results are very similar to the results from Rif1-TgWT, they were pooled (Rif1-

hem). In the table, statistically significant differences are summarized. *P* values are calculated by χ^2 test.

Figure 3. **RIF1 spatially confines chromatin contacts in a dose-dependent manner.**

A. Normalised contact frequency versus genomic distances for Hi-C reads normalised. Three biological replicas per genotype, except for Rif1-FH, are shown. *Intra*-TADs contacts (line at a median TAD's size of approximately 0.3Mbp), and long-range (over 10Mbp apart) are indicated. Shaded areas represent standard deviations.
B. Representative distribution of the median number of *in cis* chromatin contacts per indicated position (arbitrary units) within the specified region of Chromosome 11. Three independent clones per genotype were used. Upper: $\log_2$(balanced HiC signals). Lower: $\log_2$ ((balanced HiC signals (indicated line/Rif1-WT)). Red indicates a gain of interactions over Rif1-WT, while blue represents a loss.

Figure 4. **Segregation of A and B nuclear compartments is sensitive to Rif1 dosage.**

A. Top row: Saddle plot of Hi-C data, binned at 250 kb resolution for loci ranked by their replication timing. An increase in contacts of genomic positions of opposite replication timings is progressively more evident from Rif1-WT to Rif1-KO. The triplicates for each genotype (except for Rif1-FH) were combined. Lower row: Hi-C for each genotype, data normalized to Rif1-WT. Red indicates a gain in contacts.
B. Top row: Saddle plot of Hi-C data, binned at 250 kb resolution for loci ranked by their association with RIF1 (Foti et al., 2016). An increase in contacts between RIF1-associated and RIF1-devoided genomic positions is progressively more evident from Rif1-WT to Rif1-KO. The triplicates for each genotype (except for Rif1-FH) were combined. Lower row: Hi-C for each genotype, data normalized to Rif1-WT. Red indicates a gain in contacts.
C. Principle component analysis of A/B compartmentalisation for the indicated genotypes in triplicate, except for Rif1-FH.
D. Distribution of genomic regions of 250kb windows between the A and B compartment. Average of three biological replicates is shown, except for the parental line Rif1-FH.
E. Top row: Saddle plot of Hi-C data, binned at 250 kb resolution for loci ranked by their eigenvector values. An increase in contacts between genomic positions in different compartments is progressively more evident from Rif1-WT to Rif1-KO. The triplicates for each genotype (except for Rif1-FH) were combined. Lower row: Hi-C for each genotype, data normalized by Rif1-WT. Red indicates a gain in contacts.
F. Compartment strength variation with distance for the indicated genotypes. Individual values for the three biological replicates are represented by the outlined circles, except for Rif1-FH. The bars represent standard deviations.

References

Alver, R.C., Chadha, G.S., Gillespie, P.J., and Blow, J.J. (2017). Reversal of DDK-Mediated MCM Phosphorylation by Rif1-PP1 Regulates Replication Initiation and Replisome Stability Independently of ATR/Chk1. Cell Rep *18*, 2508-2520.

Bhowmick, R., Thakur, R.S., Venegas, A.B., Liu, Y., Nilsson, J., Barisic, M., and Hickson, I.D. (2019). The RIF1-PP1 Axis Controls Abscission Timing in Human Cells. Curr Biol *29*, 1232-1242 e1235.

Buonomo, S.B., Wu, Y., Ferguson, D., and de Lange, T. (2009). Mammalian Rif1 contributes to replication stress survival and homology-directed repair. The Journal of cell biology *187*, 385-398.

Chagin, V.O., Casas-Delucchi, C.S., Reinhart, M., Schermelleh, L., Markaki, Y., Maiser, A., Bolius, J.J., Bensimon, A., Fillies, M., Domaing, P.*, et al.* (2016). 4D Visualization of replication foci in mammalian cells corresponding to individual replicons. Nat Commun *7*, 11231.

Chapman, J.R., Barral, P., Vannier, J.B., Borel, V., Steger, M., Tomas-Loba, A., Sartori, A.A., Adams, I.R., Batista, F.D., and Boulton, S.J. (2013). RIF1 is essential for 53BP1-dependent nonhomologous end joining and suppression of DNA double-strand break resection. Molecular cell *49*, 858-871.

Collart, C., Allen, G.E., Bradshaw, C.R., Smith, J.C., and Zegerman, P. (2013). Titration of four replication factors is essential for the Xenopus laevis midblastula transition. Science (New York, NY *341*, 893-896.

Cornacchia, D., Dileep, V., Quivy, J.P., Foti, R., Tili, F., Santarella-Mellwig, R., Antony, C., Almouzni, G., Gilbert, D.M., and Buonomo, S.B. (2012). Mouse Rif1 is a key regulator of the replication-timing programme in mammalian cells. The EMBO journal *31*, 3678-3690.

Daley, J.M., and Sung, P. (2013). RIF1 in DNA break repair pathway choice. Molecular cell *49*, 840-841.

Dan, J., Liu, Y., Liu, N., Chiourea, M., Okuka, M., Wu, T., Ye, X., Mou, C., Wang, L., Wang, L.*, et al.* (2014). Rif1 maintains telomere length homeostasis of ESCs by mediating heterochromatin silencing. Dev Cell *29*, 7-19.

Dave, A., Cooley, C., Garg, M., and Bianchi, A. (2014). Protein Phosphatase 1 Recruitment by Rif1 Regulates DNA Replication Origin Firing by Counteracting DDK Activity. Cell Rep *7*, 53-61.

Daxinger, L., Harten, S.K., Oey, H., Epp, T., Isbel, L., Huang, E., Whitelaw, N., Apedaile, A., Sorolla, A., Yong, J.*, et al.* (2013). An ENU mutagenesis screen identifies novel and known genes involved in epigenetic processes in the mouse. Genome Biol *14*, R96.

Di Virgilio, M., Callen, E., Yamane, A., Zhang, W., Jankovic, M., Gitlin, A.D., Feldhahn, N., Resch, W., Oliveira, T.Y., Chait, B.T.*, et al.* (2013). Rif1 prevents resection of DNA breaks and promotes immunoglobulin class switching. Science (New York, NY *339*, 711-715.

Dileep, V., Ay, F., Sima, J., Vera, D.L., Noble, W.S., and Gilbert, D.M. (2015). Topologically associating domains and their long-range contacts are established during early G1 coincident with the establishment of the replication-timing program. Genome Res *25*, 1104-1113.

Dimitrova, D.S., and Gilbert, D.M. (1999). The spatial position and replication timing of chromosomal domains are both established in early G1 phase. Molecular cell *4*, 983-993.

Feng, L., Fong, K.W., Wang, J., Wang, W., and Chen, J. (2013). RIF1 counteracts BRCA1-mediated end resection during DNA repair. The Journal of biological chemistry *288*, 11135-11143.

Foti, R., Gnan, S., Cornacchia, D., Dileep, V., Bulut-Karslioglu, A., Diehl, S., Buness, A., Klein, F.A., Huber, W., Johnstone, E.*, et al.* (2016). Nuclear Architecture Organized by Rif1 Underpins the Replication-Timing Program. Molecular cell *61*, 260-273.

Fox, M.H., Arndt-Jovin, D.J., Jovin, T.M., Baumann, P.H., and Robert-Nicoud, M. (1991). Spatial and temporal distribution of DNA replication sites localized by immunofluorescence and confocal microscopy in mouse fibroblasts. Journal of cell science *99 (Pt 2)*, 247-253.

Gallardo, F., Laterreur, N., Cusanelli, E., Ouenzar, F., Querido, E., Wellinger, R.J., and Chartrand, P. (2011). Live cell imaging of telomerase RNA dynamics reveals cell cycle-dependent clustering of telomerase at elongating telomeres. Molecular cell *44*, 819-827.

Gupta, R., Somyajit, K., Narita, T., Maskey, E., Stanlie, A., Kremer, M., Typas, D., Lammers, M., Mailand, N., Nussenzweig, A.*, et al.* (2018). DNA Repair Network Analysis Reveals Shieldin as a Key Regulator of NHEJ and PARP Inhibitor Sensitivity. Cell *173*, 972-988 e923.

Hardy, C.F., Sussel, L., and Shore, D. (1992). A RAP1-interacting protein involved in transcriptional silencing and telomere length regulation. Genes & development *6*, 801-814.

Hayano, M., Kanoh, Y., Matsumoto, S., Renard-Guillet, C., Shirahige, K., and Masai, H. (2012). Rif1 is a global regulator of timing of replication origin firing in fission yeast. Genes & development *26*, 137-150.

Hengeveld, R.C., de Boer, H.R., Schoonen, P.M., de Vries, E.G., Lens, S.M., and van Vugt, M.A. (2015). Rif1 Is Required for Resolution of Ultrafine DNA Bridges in Anaphase to Ensure Genomic Stability. Dev Cell *34*, 466-474.

Hiraga, S., Alvino, G.M., Chang, F., Lian, H.Y., Sridhar, A., Kubota, T., Brewer, B.J., Weinreich, M., Raghuraman, M.K., and Donaldson, A.D. (2014). Rif1 controls DNA replication by directing Protein Phosphatase 1 to reverse Cdc7-mediated phosphorylation of the MCM complex. Genes & development *28*, 372-383.

Hiraga, S.I., Ly, T., Garzon, J., Horejsi, Z., Ohkubo, Y.N., Endo, A., Obuse, C., Boulton, S.J., Lamond, A.I., and Donaldson, A.D. (2017). Human RIF1 and protein phosphatase 1 stimulate DNA replication origin licensing but suppress origin activation. EMBO Rep *18*, 403-419.

Jorgensen, H.F., Azuara, V., Amoils, S., Spivakov, M., Terry, A., Nesterova, T., Cobb, B.S., Ramsahoye, B., Merkenschlager, M., and Fisher, A.G. (2007). The impact of chromatin modifiers on the timing of locus replication in mouse embryonic stem cells. Genome Biol *8*, R169.

Kaaij, L.J.T., van der Weide, R.H., Ketting, R.F., and de Wit, E. (2018). Systemic Loss and Gain of Chromatin Architecture throughout Zebrafish Development. Cell Rep *24*, 1-10 e14.

Kanoh, Y., Matsumoto, S., Fukatsu, R., Kakusho, N., Kono, N., Renard-Guillet, C., Masuda, K., Iida, K., Nagasawa, K., Shirahige, K.*, et al.* (2015). Rif1 binds to G quadruplexes and suppresses replication over long distances. Nature structural & molecular biology *22*, 889-897.

Kobayashi, S., Fukatsu, R., Kanoh, Y., Kakusho, N., Matsumoto, S., Chaen, S., and Masai, H. (2019). Both a Unique Motif at the C Terminus and an N-Terminal HEAT Repeat Contribute to G-Quadruplex Binding and Origin Regulation by the Rif1 Protein. Molecular and cellular biology *39*.

Li, J., Santoro, R., Koberna, K., and Grummt, I. (2005). The chromatin remodeling complex NoRC controls replication timing of rRNA genes. The EMBO journal *24*, 120-127.

Li, P., Wang, L., Bennett, B.D., Wang, J., Li, J., Qin, Y., Takaku, M., Wade, P.A., Wong, J., and Hu, G. (2017). Rif1 promotes a repressive chromatin state to safeguard against endogenous retrovirus activation. Nucleic acids research *45*, 12723-12738.

Martina, M., Bonetti, D., Villa, M., Lucchini, G., and Longhese, M.P. (2014). Saccharomyces cerevisiae Rif1 cooperates with MRX-Sae2 in promoting DNA-end resection. EMBO Rep *15*, 695-704.

Mattarocci, S., Reinert, J.K., Bunker, R.D., Fontana, G.A., Shi, T., Klein, D., Cavadini, S., Faty, M., Shyian, M., Hafner, L.*, et al.* (2017). Rif1 maintains telomeres and mediates DNA repair by encasing DNA ends. Nature structural & molecular biology *24*, 588-595.

Mattarocci, S., Shyian, M., Lemmens, L., Damay, P., Altintas, D.M., Shi, T., Bartholomew, C.R., Thoma, N.H., Hardy, C.F., and Shore, D. (2014). Rif1 Controls DNA Replication Timing in Yeast through the PP1 Phosphatase Glc7. Cell Rep *7*, 62-69.

Mirman, Z., Lottersberger, F., Takai, H., Kibe, T., Gong, Y., Takai, K., Bianchi, A., Zimmermann, M., Durocher, D., and de Lange, T. (2018). 53BP1-RIF1-shieldin counteracts DSB resection through CST- and Polalpha-dependent fill-in. Nature *560*, 112-116.

Moindrot, B., Audit, B., Klous, P., Baker, A., Thermes, C., de Laat, W., Bouvet, P., Mongelard, F., and Arneodo, A. (2012). 3D chromatin conformation correlates with replication timing and is conserved in resting cells. Nucleic acids research *40*, 9470-9481.

Moriyama, K., Lai, M.S., and Masai, H. (2017). Interaction of Rif1 Protein with G-Quadruplex in Control of Chromosome Transactions. Advances in experimental medicine and biology *1042*, 287-310.

Moriyama, K., Yoshizawa-Sugata, N., and Masai, H. (2018). Oligomer formation and G-quadruplex binding by purified murine Rif1 protein, a key organizer of higher-order chromatin architecture. The Journal of biological chemistry *293*, 3607-3624.

Muller, I., Boyle, S., Singer, R.H., Bickmore, W.A., and Chubb, J.R. (2010). Stable morphology, but dynamic internal reorganisation, of interphase human chromosomes in living cells. PLoS One *5*, e11560.

Nagano, T., Lubling, Y., Varnai, C., Dudley, C., Leung, W., Baran, Y., Mendelson Cohen, N., Wingett, S., Fraser, P., and Tanay, A. (2017). Cell-cycle dynamics of chromosomal organization at single-cell resolution. Nature *547*, 61-67.

Nakamura, H., Morita, T., and Sato, C. (1986). Structural organizations of replicon domains during DNA synthetic phase in the mammalian nucleus. Experimental cell research *165*, 291-297.

Nakayasu, H., and Berezney, R. (1989). Mapping replicational sites in the eucaryotic cell nucleus. The Journal of cell biology *108*, 1-11.

Noordermeer, S.M., Adam, S., Setiaputra, D., Barazas, M., Pettitt, S.J., Ling, A.K., Olivieri, M., Alvarez-Quilon, A., Moatti, N., Zimmermann, M.*, et al.* (2018). The shieldin complex mediates 53BP1-dependent DNA repair. Nature *560*, 117-121.

Ogiyama, Y., Schuettengruber, B., Papadopoulos, G.L., Chang, J.M., and Cavalli, G. (2018). Polycomb-Dependent Chromatin Looping Contributes to Gene Silencing during Drosophila Development. Molecular cell *71*, 73-88 e75.

Oldach, P., and Nieduszynski, C.A. (2019). Cohesin-Mediated Genome Architecture Does Not Define DNA Replication Timing Domains. Genes (Basel) *10*.

Peace, J.M., Ter-Zakarian, A., and Aparicio, O.M. (2014). Rif1 Regulates Initiation Timing of Late Replication Origins throughout the S. cerevisiae Genome. PLoS One *9*, e98501.

Pope, B.D., Ryba, T., Dileep, V., Yue, F., Wu, W., Denas, O., Vera, D.L., Wang, Y., Hansen, R.S., Canfield, T.K.*, et al.* (2014). Topologically associating domains are stable units of replication-timing regulation. Nature *515*, 402-405.

Roux, K.J., Kim, D.I., Raida, M., and Burke, B. (2012). A promiscuous biotin ligase fusion protein identifies proximal and interacting proteins in mammalian cells. The Journal of cell biology *196*, 801-810.

Ryba, T., Hiratani, I., Lu, J., Itoh, M., Kulik, M., Zhang, J., Schulz, T.C., Robins, A.J., Dalton, S., and Gilbert, D.M. (2010). Evolutionarily conserved replication timing profiles predict long-range chromatin interactions and distinguish closely related cell types. Genome Res *20*, 761-770.

Seller, C.A., and O'Farrell, P.H. (2018). Rif1 prolongs the embryonic S phase at the Drosophila mid-blastula transition. PLoS Biol *16*, e2005687.

Shi, T., Bunker, R.D., Mattarocci, S., Ribeyre, C., Faty, M., Gut, H., Scrima, A., Rass, U., Rubin, S.M., Shore, D.*, et al.* (2013). Rif1 and Rif2 shape telomere function and architecture through multivalent Rap1 interactions. Cell *153*, 1340-1353.

Silverman, J., Takai, H., Buonomo, S.B., Eisenhaber, F., and de Lange, T. (2004). Human Rif1, ortholog of a yeast telomeric protein, is regulated by ATM and 53BP1 and functions in the S-phase checkpoint. Genes & development *18*, 2108-2119.

Sima, J., Chakraborty, A., Dileep, V., Michalski, M., Klein, K.N., Holcomb, N.P., Turner, J.L., Paulsen, M.T., Rivera-Mulia, J.C., Trevilla-Garcia, C.*, et al.* (2019). Identifying cis Elements for Spatiotemporal Control of Mammalian DNA Replication. Cell *176*, 816-830 e818.

Spies, J., Lukas, C., Somyajit, K., Rask, M.B., Lukas, J., and Neelsen, K.J. (2019). 53BP1 nuclear bodies enforce replication timing at under-replicated DNA to limit heritable DNA damage. Nature cell biology *21*, 487-497.

Sukackaite, R., Cornacchia, D., Jensen, M.R., Mas, P.J., Blackledge, M., Enervald, E., Duan, G., Auchynnikava, T., Kohn, M., Hart, D.J.*, et al.* (2017). Mouse Rif1 is a regulatory subunit of protein phosphatase 1 (PP1). Sci Rep *7*, 2119.

Sukackaite, R., Jensen, M.R., Mas, P.J., Blackledge, M., Buonomo, S.B., and Hart, D.J. (2014). Structural and Biophysical Characterization of Murine Rif1 C Terminus Reveals High Specificity for DNA Cruciform Structures. The Journal of biological chemistry.

Takebayashi, S., Lei, I., Ryba, T., Sasaki, T., Dileep, V., Battaglia, D., Gao, X., Fang, P., Fan, Y., Esteban, M.A.*, et al.* (2013). Murine esBAF chromatin remodeling complex subunits BAF250a and Brg1 are necessary to maintain and reprogram pluripotency-specific replication timing of select replication domains. Epigenetics Chromatin *6*, 42.

Tanaka, H., Muto, A., Shima, H., Katoh, Y., Sax, N., Tajima, S., Brydun, A., Ikura, T., Yoshizawa, N., Masai, H.*, et al.* (2016). Epigenetic Regulation of the Blimp-1 Gene (Prdm1) in B Cells Involves Bach2 and Histone Deacetylase 3. The Journal of biological chemistry *291*, 6316-6330.

Teixeira, M.T., Arneric, M., Sperisen, P., and Lingner, J. (2004). Telomere length homeostasis is achieved via a switch between telomerase- extendible and -nonextendible states. Cell *117*, 323-335.

Toteva, T., Mason, B., Kanoh, Y., Brogger, P., Green, D., Verhein-Hansen, J., Masai, H., and Thon, G. (2017). Establishment of expression-state boundaries by Rif1 and Taz1 in fission yeast. Proceedings of the National Academy of Sciences of the United States of America *114*, 1093-1098.

Vogelauer, M., Rubbi, L., Lucas, I., Brewer, B.J., and Grunstein, M. (2002). Histone acetylation regulates the time of replication origin firing. Molecular cell *10*, 1223-1233.

Xu, D., Muniandy, P., Leo, E., Yin, J., Thangavel, S., Shen, X., Ii, M., Agama, K., Guo, R., Fox, D., 3rd*, et al.* (2010). Rif1 provides a new DNA-binding interface for the Bloom syndrome complex to maintain normal replication. The EMBO journal *29*, 3140-3155.

Yaffe, E., Farkash-Amar, S., Polten, A., Yakhini, Z., Tanay, A., and Simon, I. (2010). Comparative analysis of DNA replication timing reveals conserved large-scale chromosomal architecture. PLoS Genet *6*, e1001011.

Yamazaki, S., Ishii, A., Kanoh, Y., Oda, M., Nishito, Y., and Masai, H. (2012). Rif1 regulates the replication timing domains on the human genome. The EMBO journal *31*, 3667-3677.

Yang, B.X., El Farran, C.A., Guo, H.C., Yu, T., Fang, H.T., Wang, H.F., Schlesinger, S., Seah, Y.F., Goh, G.Y., Neo, S.P.*, et al.* (2015). Systematic identification of factors for provirus silencing in embryonic stem cells. Cell *163*, 230-245.

Yokochi, T., Poduch, K., Ryba, T., Lu, J., Hiratani, I., Tachibana, M., Shinkai, Y., and Gilbert, D.M. (2009). G9a selectively represses a class of late-replicating genes at the nuclear periphery. Proceedings of the National Academy of Sciences of the United States of America *106*, 19363-19368.

Yoshida, K., Bacal, J., Desmarais, D., Padioleau, I., Tsaponina, O., Chabes, A., Pantesco, V., Dubois, E., Parrinello, H., Skrzypczak, M.*, et al.* (2014). The histone deacetylases sir2 and rpd3 act on ribosomal DNA to control the replication program in budding yeast. Molecular cell *54*, 691-697.

Zhang, H., Petrie, M.V., He, Y., Peace, J.M., Chiolo, I.E., and Aparicio, O.M. (2019). Dynamic relocalization of replication origins by Fkh1 requires execution of DDK function and Cdc45 loading at origins. Elife *8*.

Zofall, M., Smith, D.R., Mizuguchi, T., Dhakshnamoorthy, J., and Grewal, S.I.S. (2016). Taz1-Shelterin Promotes Facultative Heterochromatin Assembly at Chromosome-Internal Sites Containing Late Replication Origins. Molecular cell *62*, 862-874.

METHODS

Mouse embryonic stem cell derivation

Mouse embryonic stem cell (ESC) cells were derived as described in (Foti, Gnan et al. 2016), with the addition of 1 µM MEK inhibitor PD0325901 and 3 µM GSK3 inhibitor CHIR99021 (MRC PPU Reagents and Services, School of Life Sciences, The University of Dundee) in the culture media, from the start of the protocol.
Rif1$^{FH/flox}$ Rosa26$^{Cre\text{-}ERT/+}$ ESCs were derived by crossing Rif1$^{flox/+}$ Rosa26$^{Cre\text{-}ERT/Cre\text{-}}$ERT (Buonomo, Wu et al. 2009) with Rif1$^{FH/FH}$ (Cornacchia, Dileep et al. 2012) mice. The Rif1^{FH} allele was specifically targeted in the parental line Rif1$^{FH/flox}$ Rosa26$^{Cre\text{-}ERT/+}$ (Rif1-FH). Integrants were selected by hygromycin resistance. The targeting vector encodes for a codon-optimized cDNA of RIF1 (exon 8 to exon 36). Hygromycin-resistant colonies were screened for correct targeting of the Rif1^{FH} allele by Southern blot (EcoRV digest) and using a PCR-amplified probe (primers in Table 1).

Cell manipulation

ESCs were grown at 37°C in 7.5 % CO_2 in Knockout DMEM (Gibco 10829-018), containing 12.5% heat-inactivated fetal bovine serum (Pan-Biotech), 1 % non-essential amino acids (Gibco 11140-035), 1% Penicillin/Streptomycin (Gibco 15070063), 0.1 mM 2-Mercaptoethanol (Gibco 31350-010), 1% L-Glutamine (Gibco 25030024)), supplemented with 1 µM PD0325901 and 3 µM CHIR99021 and 20 ng/ml leukemia inhibitory factor (LIF, EMBL Protein Expression and Purification core facility).
Experiments were carried out each time from a frozen vial of cells, at least two passages after thawing. $5.2 \cdot 10^6$ cells for Rif1-WT and $6.5 \cdot 10^6$ for Rif1-KO lines, per 15 cm plate (or the equivalent for different sized plates) were plated at day zero, when treatment with 200 nM 4-hydroxytamoxifen (OHT, Sigma H7904) started. Fresh medium with OHT was added after 48 hours. Cells were collected about 96 hours after starting OHT treatment.

Replication Timing analysis

Cells were pulsed for 2 hours with 10 µM BrdU, collected and fixed in 70 % ethanol. Processing was as described in (Ryba, Hiratani et al. 2011). Fastq files were aligned using Bowtie2 version 2.2.6 on mm10 as a reference genome. SAM files were converted into BAM files and sorted using Samtools version: 1.3.1. bamCompare version 3.1.3 was used to create bedgraph files with 50 kb and 1 kb binning of the $\log_2$ ratio of the early and late fraction. Duplicated reads were excluded from the computation of the bedgraph files as well as reads mapped on XY chromosomes. The two fractions were normalized as reads per millions (RPM). Plots and data manipulation were carried out R version 3.5.1. The original names of the cell lines used in these experiments, included in the name of the Repli-seq raw files are: RFHF14 = Rif1-FH, 14 tgWT A7 = Rif1-TgWT 1, 14 tgWT H4 = Rif1-TgWT 2, 14 tgwt H6 = Rif1-TgWT 3, 14 ΔP G11 = Rif1-ΔPP1 1, 14 ΔP H1 = Rif1-ΔPP1 2, 14 ΔP H2 = Rif1-ΔPP1 3, ESC B = Rif1-WT 1, ESC F = Rif1-WT 2, ESC H = Rif1-WT 3, ESC 5 = Rif1-KO 1, ESC 18 = Rif1-KO 2, ESC 24 = Rif1-KO 3.

Cell cycle distribution analysis

After four days of OHT treatment, cells were pulsed for 30 minutes with 10 µM EdU (Invitrogen A10044). Cells were then washed with cold DPBS (Thermo Fisher Scientific 14190094), collected, counted and fixed in 75 %. EtOH Samples were kept at -20 ^{o}C for at least overnight. $7.5 \cdot 10^5$ cells were then processed for click-chemistry detection of EdU. After washing in cold DPBS, cells were permeabilised in DPBS/1% FBS/0.01 % Triton X-100 (Sigma93426-250ML) for 10 minutes on ice. After washing twice, cells were incubated in 900 µl of DPBS with 10 mM Na-Ascorbate (Sigma A7631-25G), 1 µM Alexa Fluor 647 Azide (Thermo Fisher Scientific A10277) and $CuSO_4$ 0.1 M (Sigma C1297) for 30 minutes at room temperature in the dark, rotating. Cells were washed in DPBS/1%FBS/0.5% Tween 20 (Sigma P9416-100ML) for 10 minutes and then twice in cold DPBS/1% FBS. After 1 hour incubation in 300 µl of DPBS/1%FBS /DAPI 2.5 g/ml (Thermo Fisher Scientific D1306), the samples were analyzed using an LSR II FACS (BD). The data acquired were analysed using Flowjo software and plotted in R 3.5.1.

Intra-cellular FACS staining for ^{HA}Rif1

After four days of OHT treatment, cells were collected and counted. $3 \cdot 10^6$ cells were fixed in 400 µl of DPBS/2% Paraformaldehyde (Sigma P-6148) for 10 minutes at room temperature shaking. Paraformaldehyde was then diluted to 0.2% and next cells were washed in cold DPBS. After 2 minutes permeabilisation in 200 µl PBS-Triton X-100 0.1%, cells were incubated 5 minutes in saponin solution (COMPONENT E from kit C10424, Thermo Fisher Scientific) at room temperature and anti-HA antibody (Covance monoclonal HA.11 clone 16B12 #MMS-101R, RRID:AB_291262) was added at 1:500. After 1 hour at room temperature rotating, cells were washed twice in DPBS/2% FBS, resuspended in 200 µl of saponin solution with goat anti-mouse Alexa Fluor 647 1:1000 (Thermo Fisher Scientific A-21235, RRID:AB_2535804) and incubated for 1 hour rotating in the dark. After washing twice samples were resuspended in 400 µl of saponin solution with DAPI 2.5 g/ml (Thermo Fisher Scientific D1306) and analyzed on an LSR II FACS (BD). Data were processed using R version 3.5.1.

Hi-C

After four days of OHT treatment, cells were collected and counted. Cells were washed twice in cold DPBS and resuspended in full media. Samples were crosslinked for 10 minutes rotating at room temperature in 1% formaldehyde (10^6 cells/ml). Crosslinking was stopped by adding glycine at the final concentration of 0.2 M for 5 minutes at RT. Samples were washed twice in cold DPBS and pellets were snap frozen. 2-5 × 10^6 cells per sample were lysed in 10 mM Tris-HCl pH 8.0, 10 mM NaCl, 0.2% IGEPAL (Sigma, I3021) supplemented with protease inhibitor (Thermo Scientific, 78430) for 15 minutes on ice. Nuclei were washed twice in cold lysis buffer, resuspended in 50 µl of NEBuffer 3.1 (NEB, B7003S) supplemented with 0.3% SDS and incubated at 62°C for 10 minutes. After diluting and quenching the SDS by adding 57.5 µl of NEBuffer 3 and 12.5 µl of 20% Triton X-100 (Sigma, 93443), samples were incubated at 37°C for 60 minutes. Nuclei were spun and incubated in 250 µl of 1× DpnII buffer with 600 U of DpnII restriction enzyme (NEB, R0543L) overnight at 37°C. An additional 200 U of DpnII were added to each sample the following day and incubated for a further 2 hours.
After heat inactivation of DpnII for 20 min at 65°C, restriction fragments ends were filled by DNA polymerase I, Large (Klenow) Fragment (NEB, M0210), 0.8 U/µl of DNA, in 50 µl of 0.3 mM biotin-14-dATP (Thermo Fisher, 19524016), 0.3 mM dCTP/ dGTP/ dTTP for 1.5 hours at 37°C.

900 µl of ligation master mix were then add to the samples: 1.33x NEB T4 DNA ligase buffer (NEB, B0202), 1.1% Triton X-100, 1.33 mg of Bovine Serum Albumin and 2000 U of T4 DNA Ligase (NEB, M0202). Samples were incubated for 4 hours rotating. Nuclei were spun and resuspended in water and digested with proteinase K (Sigma, P6556) 1.2 mg/ml and 0.8% SDS at 55°C for 30 minutes. 130 µl of 5 M NaCl were added and samples were incubated at 65°C overnight. After ethanol precipitation, DNA was resuspended in 500 µl of 10 mM Tris-HCl pH8.0 and washed trice using the same buffer using Amicon filters (Millipore, UFC503096). Samples were diluted in 50 mM Tris pH 8.0, 0.1% SDS, 10 mM EDTA and sonicated to about 500 bp using a probe-based sonicator. Washes were then repeated as in the previous step. Biotinylated DNA was pulled down using 30 µl of 10 mg/ml Dynabeads MyOne Streptavidin T1 beads (Life technologies, 65602) in 10 mM Tris-HCl (pH 7.5); 1 mM EDTA; 2 M NaCl for 15 minutes at room temperature rotating. Beads were washed in TWB: 5 mM Tris-HCl (pH 7.5); 0.5 mM EDTA; 1 M NaCl; 0.05% Tween 20 for 2 minutes at 55° C twice, resuspended in 20 µl 1× NEB T4 DNA ligase buffer, transferred to a new tube and incubated for 30 minutes at room temperature with 100 µl of: 1x NEB T4 DNA ligase buffer, 0.5 mM dNTPs, 50 U T4 PNK (NEB, M0201), 12 U T4 DNA polymerase I (NEB, M0203), 5 U DNA polymerase I, Large (Klenow) Fragment. After two washes in TWB at 55°C for 2 minutes, beads were transferred to 1× NEBuffer 2 (NEB, B7002S) and moved to a new tube. Beads were then incubated at 37°C for 30 minutes in 100 µl of 0.9X NEBuffer 2, 0.5 mM dATP and 25 U Klenow exo minus (NEB, M0212). Beads were washed again as before and transferred to T4 ligation buffer. DNA was ligated for 2.5 hours with Illumina adaptors in 50 µl of the following reaction mix: 1X T4 ligation buffer, 1.2 µM Illumina adaptors, 1U T4 DNA ligase. Beads were washed once again with TWB as before, to be then resuspended and stored in 50 µl of 10 mM Tris-HCl (pH8.0).
Libraries were amplified in six parallel 50 µl PCR reactions using Illumina primers and 4 µl of beads (or DNA removed off the beads by heating at 95°C for 20 min) per reaction after testing optimal amplification cycles. Size selection was performed on an agarose gel, isolating fragments between 300-700 base pairs, followed by purification with QIAquick Gel Extraction Kit (Qiagen 28704). Each library was sequenced on one lane of Illumina Nex-seq 500/550 (75 bp paired end reads). FASTQ files were processed with the distiller pipeline (https://github.com/mirnylab/distiller-nf, DOI:10.5281/zenodo.2630563) to obtain *.mcool* files used in downstream analyses.

Protein extraction

Cells were washed twice in cold DPBS and resuspended in hypotonic buffer: 25 mM Tris-HCl (pH 7.4); 50 mM KCl; 2 mM $MgCl_2$; 1 mM EDTA, proteinase inhibitor (Roche, 5056489001) at the concentration of $20 \cdot 10^6$ cells/ml. Samples were incubated for 20 minutes on ice, washed twice with hypotonic buffer and resuspended in the same volume of Benzonase buffer: 50 mM Tris-HCl (pH 8.0); 100 mM NaCl; 1.5 mM MgCl2; 10 % Glycerol; proteinase inhibitor (Roche, 5056489001). After 3 cycles of snap freezing and thawing, samples were supplemented with 50 U/ ml of benzonase (Sigma, E1014) and incubated at room temperature for 25 minutes. 0.2 % Triton X-100 was added and samples were incubated for 10 minutes at 4°C rotating. After centrifugation, supernatant was collected and quantified by Bradford (Bradford 1976) (Biorad, 5000006). Immunoprecipitation was performed, SDS-Page and Western Blot analysis were performed as in Foti et al. 2016.

RNA extraction and qRT-PCR.

Total RNA was extracted using RNeasy kit (QIAGEN, 74106) according to manufacturer's instructions. cDNA synthesis was performed using RevertAid H Minus reverse transcriptase (Thermo Scientific, K1632) and qPCR was performed using the SYBR Green reaction mix (Roche, 04887352001) on a LightCycler 96 Instrument. Gene expression data was normalized against GAPDH and the relative RNA expression levels were calculated using the Ct ($2^{\Delta\Delta Ct}$) method.

3D-SIM and image analysis

Cells were split on a coverslip on the 4th day of OHT treatment and after 5 hours after splitting were pulsed with 10µM BrdU for 15 minutes. After 2x washes in PBS at 37°C, cells were chased for 3 hours in CO_2 pre-equilibrated, medium at 37°C. After 2x washes in PBS, cells were fixed for 10 minutes in methanol free 3.7% formaldehyde. For immunostaining, fixed cells were permeabilised for 15 minutes in 0.5% TritonX-100/PBS, blocked for 30 minutes in 0.02% Tween 20/PBS/2% BSA, and stained with anti BrdU antibody (Biomol, Rockland, 600-401-C29, RRID:AB_10893609) for 60 min at 37 °C. Washes were performed in PBS/0.02% Tween 20. Immunostained cells mounted in Vectashield (Vector Laboratories) were used for super resolution imaging. Samples were acquired on a 3D-SIM Deltavision OMX V3 microscope (General Electric) equipped with a 100 × 1.4 oil immersion objective UPlanSApo (Olympus), 405 nm, 488 nm and 593 nm diode lasers and Cascade II EMCCD cameras (Photometrics). After acquisition, the 3D-SIM raw data were first reconstructed and corrected for colour shifts with the help of the provided software softWoRx 6.0 Beta 19 (unreleased). Pseudo-widefield images were generated and exported during reconstruction too. In a second step, a custom-made macro in Fiji (Schindelin, Arganda-Carreras et al. 2012) finalised the channel alignment and established composite TIFF stacks, that were subsequently used for image analysis. For image analysis reconstructed super resolution wide field images were merged first with the corresponding pseudo-wide field stacks using FIJI. Pseudo-widefield channels were processed to enhance the focal pattern using the following steps: Difference of Gaussians filter with sigma1 = 10 and sigma2 = 1 pixels, followed by an automatic threshold (Otsu) and subsequent setting of all pixels below the threshold to 0. In contrast the super resolution replication foci were pre-segmented using the DAPI nuclear mask, followed by an automatic threshold (Triangle algorithm) and subsequently all pixels below the threshold were assigned to a value of 0, as described in detail in (Chagin, Reinhart et al. 2015). Further quantification was performed using Volocity 6.3 (Perkin Elmer). For the super resolution channel, replication foci were detected with the following settings: Find objects, histogram based segmentation with fixed lower threshold of 1 followed by a separate touching object steps with an object guide size of 0 µm3 followed by a filtering step to remove objects < 0.0002 µm3. The corresponding pseudo wide field foci were segmented using a fixed threshold of 1 and touching objects were separated with a guide size of 0.02 µm3. Finally, the pseudo wide filed foci were filtered to remove foci < 0.02 µm3. As a last step for each pseudo wide filed focus the overlapping super resolution foci (nano RFis) were calculated, based on the volume overlaps.

Click-it reaction and Immunofluorescence

mESCs were grown on gelatinized coverslips overnight. EdU (5-ethynyl-2´-deoxyuridine-Invitrogen A10044) was added to culture medium to 10 μM final concentration and incubated for 30 minutes. After PBS washes, cells were pre-extracted with Triton buffer (0.5 % Triton X-100; 20 mM Hepes-KOH (pH7.9); 50 mM NaCl; 3 mM MgCl2; 300 mM Sucrose) for 2 minutes at 4°C before fixation with 3 % paraformaldehyde-2 % sucrose for 10 minutes at room temperature. Cells were permeablised with Triton buffer for 10 minutes at RT, followed by PBS washes. After short blocking with 3% BSA/PBS for 2 minutes, Click-it reaction cocktail (as in manufacturer's instructions- Flow Cytometry Assay Kit, C10424, Invitrogen) containing Alexa Fluor 647 (Invitrogen A10277) (or Flow Cytometry Assay Kit, C10425. Invitrogen) containing Alexa Fluor 488 azide (Invitrogen, A10266) was added to coverslips and incubated in dark for 30 minutes, followed by two washes with 3% BSA/PBS. Samples were blocked with PBG (0.2% (w/v) cold water fish gelatin-Sigma G-7765; 0.5% (w/v) BSA-Sigma A-2153, in PBS). Primary antibodies were diluted in PBG and then added to samples for 2-hours incubation at room temperature or 1 hour at 37C. After three PBG washes, secondary antibodies (Invitrogen) were diluted 1:800 in PBG and the incubation was in the dark for 45 min at room temperature. After PBS washes, coverslips were mounted with Vectashield with DAPI (Vector laboratories, H-1200). Images were acquired from Zeiss 880 Airyscan with 100x oil objective.

Antibodies

Antigen	Source	Cat. #	Class	Use and dilution	
HA	Biolegend	901514	Monoclonal Mouse	WB 1:1000 IF 1:3000 FACS 1:3000	
Rif1	Buonomo et al. 2009	1240	Polyclonal Rabbit	WB 1:3000	
SMC1	Bethyl	A300-055A	Polyclonal Rabbit	WB 1:10000	
BrdU	Biomol (Rockland)	600-401-C29	Polyclonal Rabbit	IF 1:300	
MCM3	Santa Cruz	sc-9850	Polyclonal Goat	IF 1:200	
PP1α	Abcam	ab52619	Polyclonal Rabbit	WB 1:1000	
H3S10ph	Millipore	06-570	Polyclonal Rabbit	IF 1:400	

Primers

Primer	**Sequence 5' – 3'**	**Reference**
MERVL F	atgggtccaggaatcaaggg	This paper
MERVL R	gcctctggagccaaaacttc	This paper
GAPDH F	tgtgagggagatgctcagtg	This paper
GAPDH R	atggccttccgtgttcctac	This paper

References

Bradford, M. M. (1976). "A rapid and sensitive method for the quantitation of microgram quantities of protein utilizing the principle of protein-dye binding." Anal Biochem **72**: 248-254.

Buonomo, S. B., Y. Wu, D. Ferguson and T. de Lange (2009). "Mammalian Rif1 contributes to replication stress survival and homology-directed repair." J Cell Biol **187**(3): 385-398.

Chagin, V. O., M. Reinhart and M. C. Cardoso (2015). "High-resolution analysis of Mammalian DNA replication units." Methods Mol Biol **1300**: 43-65.

Cornacchia, D., V. Dileep, J. P. Quivy, R. Foti, F. Tili, R. Santarella-Mellwig, C. Antony, G. Almouzni, D. M. Gilbert and S. B. Buonomo (2012). "Mouse Rif1 is a key regulator of the replication-timing programme in mammalian cells." Embo J **31**(18): 3678-3690.

Foti, R., S. Gnan, D. Cornacchia, V. Dileep, A. Bulut-Karslioglu, S. Diehl, A. Buness, F. A. Klein, W. Huber, E. Johnstone, R. Loos, P. Bertone, D. M. Gilbert, T. Manke, T. Jenuwein and S. C. Buonomo (2016). "Nuclear Architecture Organized by Rif1 Underpins the Replication-Timing Program." Mol Cell **61**(2): 260-273.

Ryba, T., I. Hiratani, T. Sasaki, D. Battaglia, M. Kulik, J. Zhang, S. Dalton and D. M. Gilbert (2011). "Replication timing: a fingerprint for cell identity and pluripotency." PLoS Comput Biol **7**(10): e1002225.

Schindelin, J., I. Arganda-Carreras, E. Frise, V. Kaynig, M. Longair, T. Pietzsch, S. Preibisch, C. Rueden, S. Saalfeld, B. Schmid, J. Y. Tinevez, D. J. White, V. Hartenstein, K. Eliceiri, P. Tomancak and A. Cardona (2012). "Fiji: an open-source platform for biological-image analysis." Nat Methods **9**(7): 676-682.

Supplemental Information

Fig. S1 Generation of ESCs expressing RIF1-ΔPP1. Related to Fig. 1.

A. In $Rif1^{FH/flox}$ ESCs, the $Rif1^{FH}$ allele was targeted. The targeting construct allows knocking-in Rif1's codon-optimised cDNA (exons 8 to 36), either wild type or carrying the SAAA/RVSF ($Rif1^{\Delta PP1}$) mutations of the SILK and RVSF motifs, residues 2128–2131 and 2150–2153. The homology arms included in the construct to target the *Rif1* locus are shaded in grey. The targeted alleles are indicated in the figure as $^{FH}Rif1^{TgWT}$ or $^{FH}Rif1^{\Delta PP1}$ respectively. Splicing between genomic-encoded exon 7 and cDNA-encoded exon 8 allows expression of Rif1-TgWT or Rif1-ΔPP1 respectively. Restriction sites and probe used to identify by Southern blot the correct insertion of the targeting construct in $Rif1^{FH}$ allele and not the $Rif1^{flox}$ allele are indicated. The map of $Rif1^{flox}$ allele indicating the expected sizes after restriction digest and Southern blot analysis is shown.
B. Southern blot confirmation of correct integration of the targeting constructs in the cell lines employed in this work.
C. Western blot analysis of RIF1 levels after four days of hydroxytamoxifen treatment, to induce Cre-mediated deletion of $Rif1^{flox}$ allele. Proteins were extracted from untagged *Rif1-WT* ($Rif1^{+/+}$); *Rif1-KO* ($Rif1^{flox/flox}$); FLAG-HA2(FH) knock-in tagged Rif1 hemizygous: *Rif1-FH* ($Rif1^{FH/flox}$); FH-tagged targeted *Rif1-TgWT* hemizygous ($Rif1^{TgWT/flox}$); FH-tagged targeted *Rif1-ΔPP1* hemizygous ($Rif1^{\Delta PP1/flox}$). Anti-mouse Rif1 polyclonal rabbit antibody 1240 (anti-RIF1) was used to detect both FH-tagged and untagged proteins. Mouse ascites 16B12 (anti-HA) detects only FH-tagged RIF1. SMC1 levels were used as loading control.

Fig. S2 Replication timing is affected by lack of RIF1 or of RIF1-PP1 interaction, not RIF1 dosage. Related to Fig. 2.

A. Principle component analysis of RT for the indicated genotypes in triplicate, except for RIF1-FH.
B. Representative RT profile from one line per genotype at 1kb resolution.
C. Relative distribution of S-phase cells (EdU positive) between DNA contents corresponding to early, mid and late replication, as determined by DAPI quantitation (FACS). The average value of three independent clones with the same, indicated genotypes is shown. Average of three experiments. Error bars indicate standard deviations. *P* values are calculated using Kruskal–Wallis test.

Fig. S3 RIF1-ΔPP1's impact on the replication-timing program does not entirely recapitulate the consequences of RIF1 loss of function. Related to Fig. 2.

Percentage of 50kb-windows changing RT from Early-to-Late S-phase (EtoL, from a positive to a negative RT value), Early-to-Earlier (to Earlier, thus more positive value value of RT), from Late-to-Early (LtoE, from a negative to a positive RT value), and from Late-to-Later S-phase (to Later, thus more negative value of RT), over increasing thresholds.

Fig. S4 Classification of dynamic spatial distribution of replication foci in mESCs. Related to Fig. 2.

A. G1, G2 and S-phase substages classification. The different stages are distinguished by the combination of EdU staining (grey), anti-MCM3 (red) and anti-histone H3 phosphorylated on Ser10 (H3S10p, green) immunofluorescence. G1 cells display a diffuse nucleoplasmic MCM3 signal, but no EdU or H3S10p signal. Early S-phase is characterised by diffuse nucleoplasmic MCM3 and EdU staining, with no H3S10p signal. In mid S-phase MCM3 and EdU signal concentrate more in the chromocenters and H3S10p starts appearing. In late S-phase there are peripheral or sparse MCM3 and EdU signals, with H3S10p signal becoming very prominent, especially at chromocenters.
B. Examples of aberrant replication patterns in *Rif1-KO* cells. H3S10p signal, together with MCM3 located at chromocenters, normally associated with mid-late S-phase EdU patterns, is in these examples associated with diffuse nucleoplasmic EdU patterns resembling early S-phase.

Fig. S5 Analysis of the number and clustering of replication forks in mESCs. Related to Fig. 2.

A. Example of image processing and workflow to evaluate the number of replication forks (nano-replication foci, nano-RFi) versus the number of fork clusters ((pseudo)-wide-field replication focus, pWF-RFi). pWF-Rfi contain usually more than one nano-RFi, but there is a fraction of nano-RFi not associated with a pWF-RFi (yellow arrowheads).
B. Number of replication forks per cell, for two independent biological replicates per genotype (except for Rif1-WT, where only one clone was analysed). The line represents the median values and the 95% confidence intervals. *P* value is calculated using Kruskal Wallis test. The forks were visualised by anti-BrdU staining and 3D-SIM image acquisition.
C. Boxplots showing the distribution of the number of replication forks per replication focus. *P* values are calculated using t test. (0.05> *P* value >0.01 == *, 0.01 >= *P* value >0.001 == **, 0.001 >= *P* value >0.0001 == ***, *P* value < 0.0001 == ****)

Figure 1

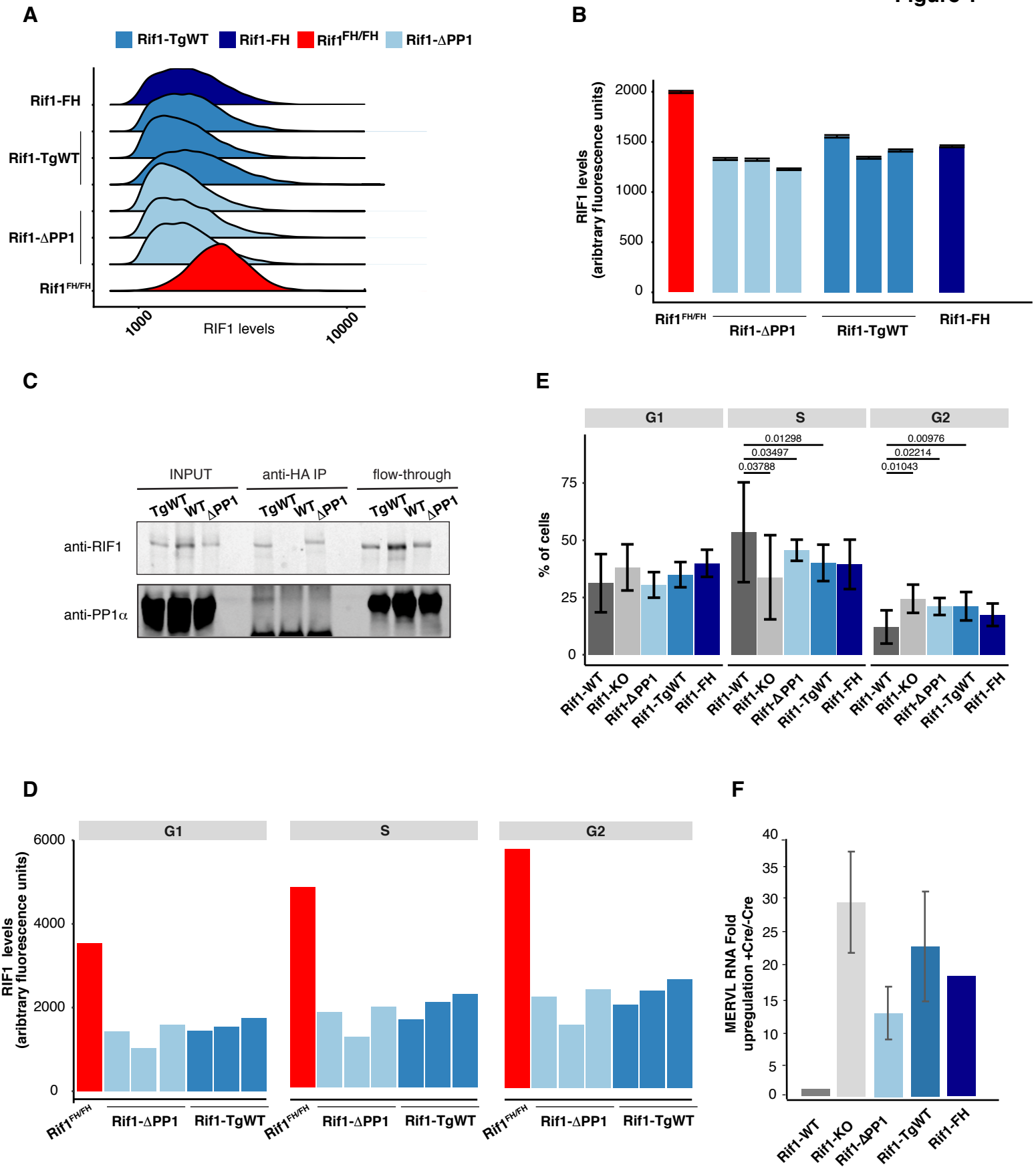
A
Rif1-TgWT
Rif1-FH
Rif1FH/FH
Rif1-ΔPP1
Rif1-FH
Rif1-TgWT
Rif1-ΔPP1
Rif1FH/FH
1000
RIF1 levels
10000
B
RIF1 levels
(aribtrary fluorescence units)
2000
1500
1000
500
0
Rif1FH/FH
Rif1-ΔPP1
Rif1-TgWT
Rif1-FH
C
INPUT
anti-HA IP
flow-through
TgWT
WT
ΔPP1
anti-RIF1
anti-PP1α
E
G1
S
G2
0.01298
0.03497
0.03788
0.00976
0.02214
0.01043
% of cells
75
50
25
0
Rif1-WT
Rif1-KO
Rif1-ΔPP1
Rif1-TgWT
Rif1-FH
D
G1
S
G2
RIF1 levels
(aribtrary fluorescence units)
6000
4000
2000
0
Rif1FH/FH
Rif1-ΔPP1
Rif1-TgWT
F
MERVL RNA Fold
upregulation +Cre/-Cre
40
35
30
25
20
15
10
5
0
Rif1-WT
Rif1-KO
Rif1-ΔPP1
Rif1-TgWT
Rif1-FH

Figure 2

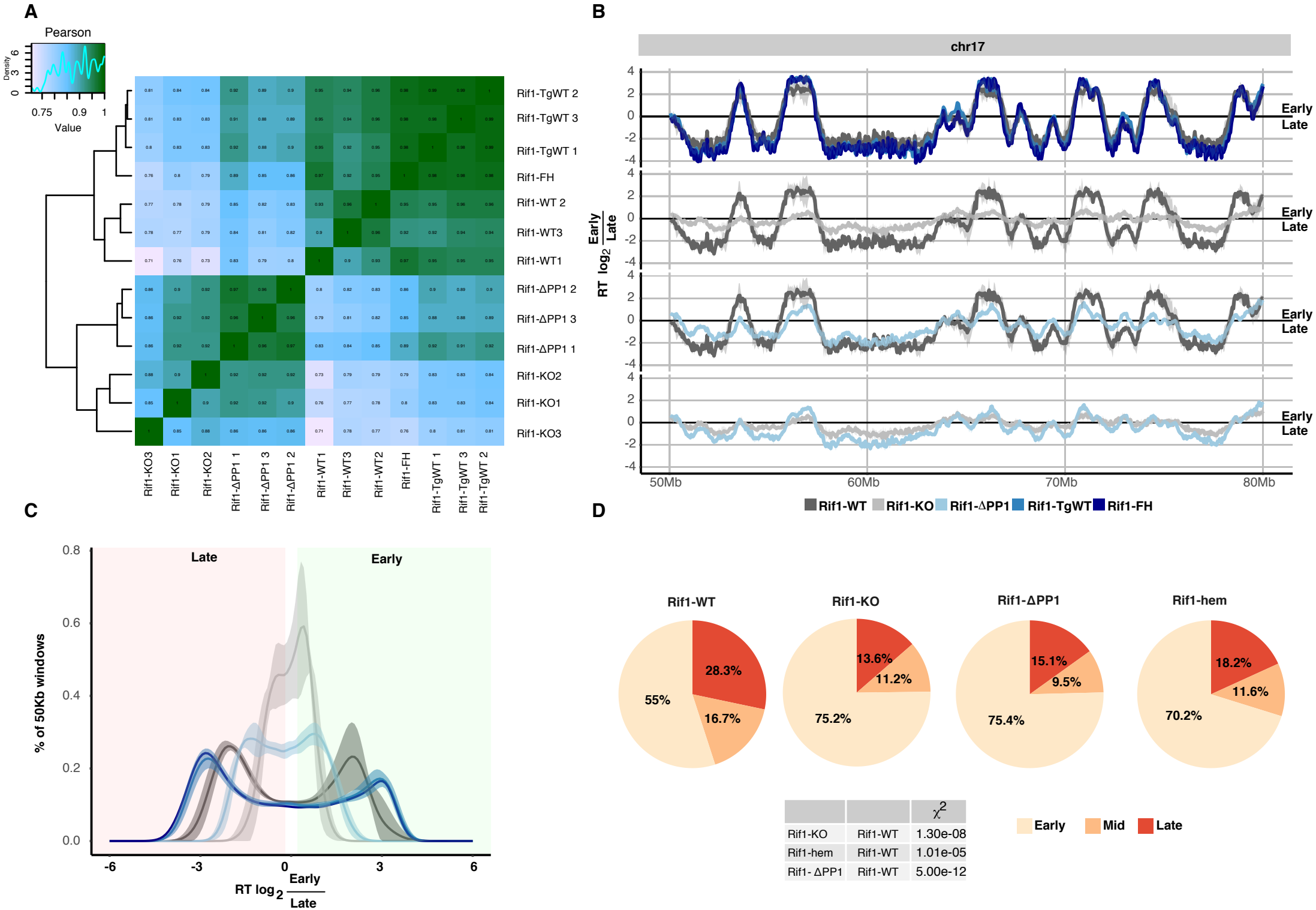

		χ^2
Rif1-KO	Rif1-WT	1.30e-08
Rif1-hem	Rif1-WT	1.01e-05
Rif1- ΔPP1	Rif1-WT	5.00e-12

Figure 3

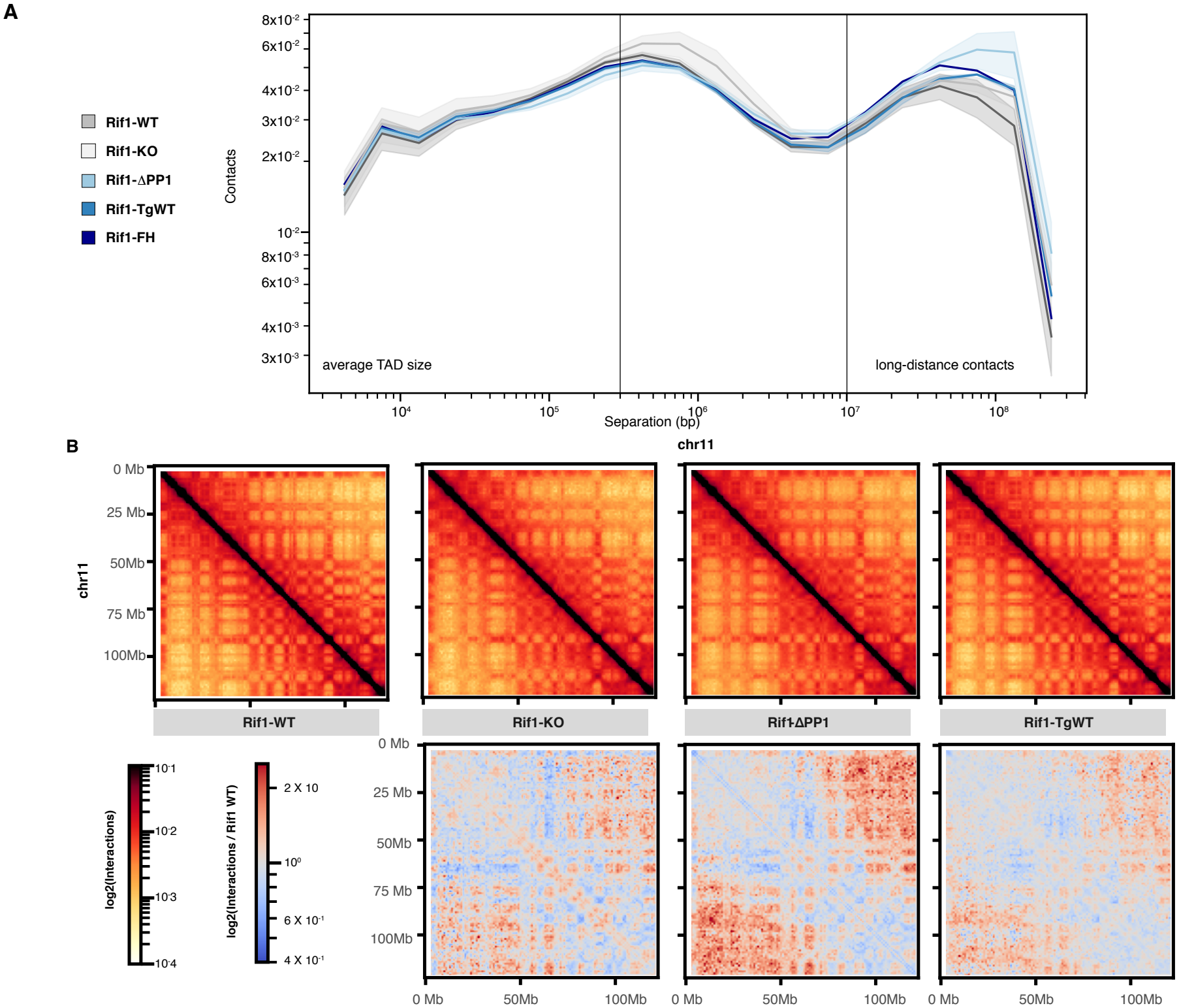
A
Rif1-WT
Rif1-KO
Rif1-ΔPP1
Rif1-TgWT
Rif1-FH
Contacts
8x10-2
6x10-2
4x10-2
3x10-2
2x10-2
10-2
8x10-3
6x10-3
4x10-3
3x10-3
average TAD size
long-distance contacts
10^4
10^5
10^6
10^7
10^8
Separation (bp)
B
chr11
0 Mb
25 Mb
50Mb
75 Mb
100Mb
Rif1-WT
Rif1-KO
Rif1-ΔPP1
Rif1-TgWT
log2(Interactions)
10-1
10-2
10-3
10-4
log2(Interactions / Rif1 WT)
2 X 10
10^0
6 X 10-1
4 X 10-1
0 Mb
50Mb
100Mb

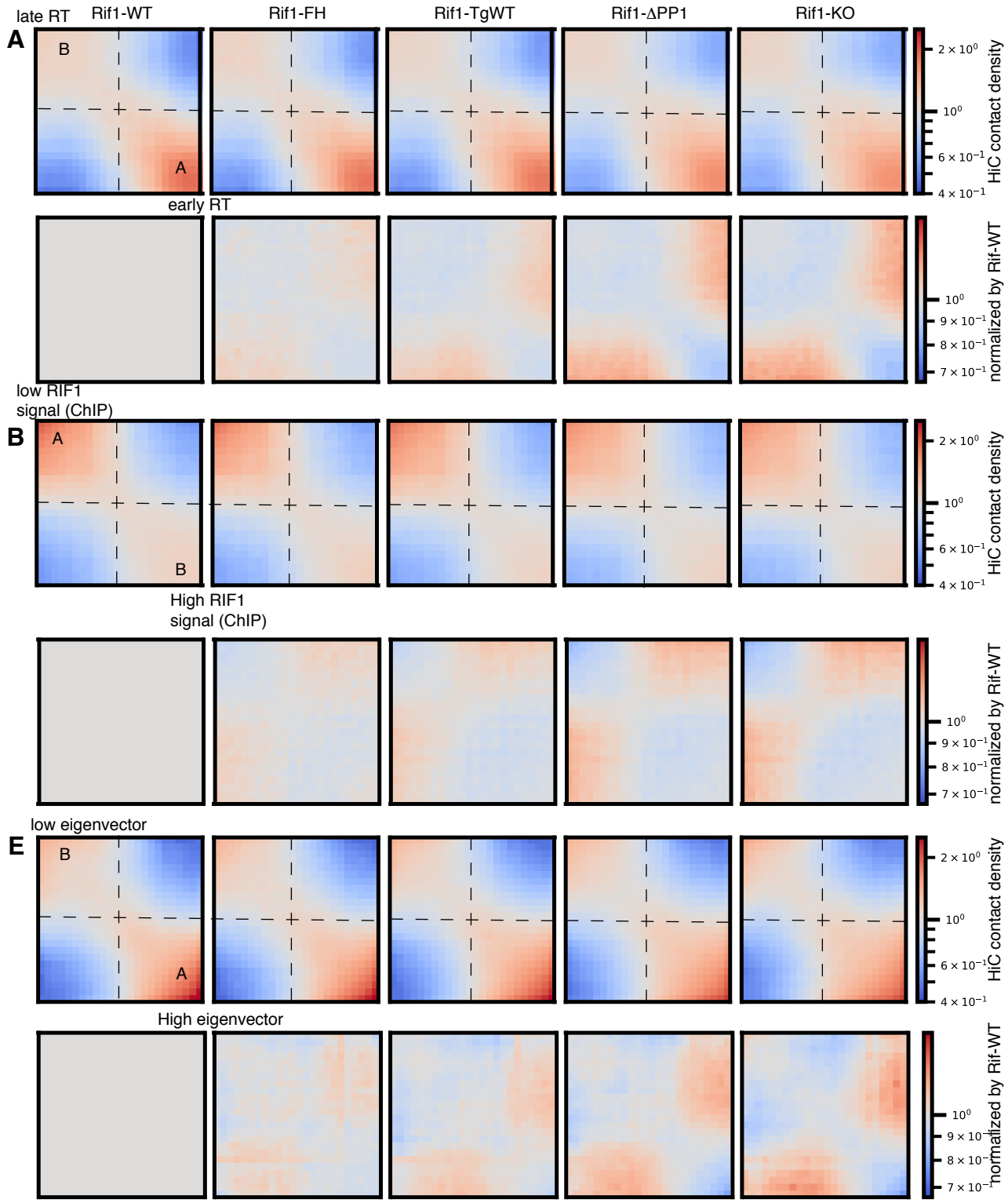
A
late RT
Rif1-WT
Rif1-FH
Rif1-TgWT
Rif1-ΔPP1
Rif1-KO
B
A
HiC contact density
early RT
normalized by Rif-WT
low RIF1 signal (ChIP)
B
A
High RIF1 signal (ChIP)
E
low eigenvector
High eigenvector

Figure 4

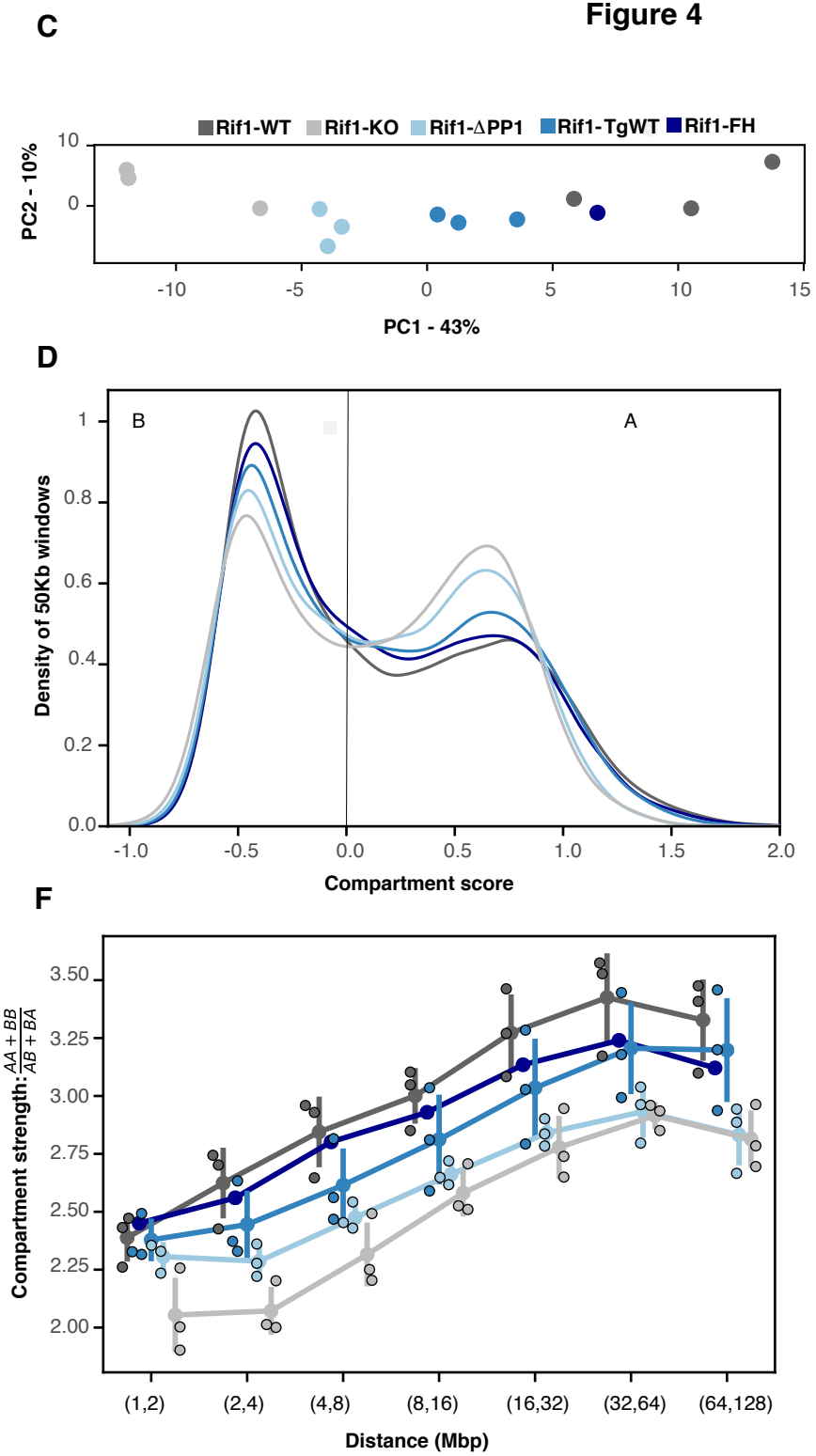
C
Rif1-WT
Rif1-KO
Rif1-ΔPP1
Rif1-TgWT
Rif1-FH
PC2 - 10%
PC1 - 43%
D
B
A
Density of 50Kb windows
Compartment score
F
Compartment strength: $\frac{AA+BB}{AB+BA}$
(1,2)
(2,4)
(4,8)
(8,16)
(16,32)
(32,64)
(64,128)
Distance (Mbp)

Figure S1

A

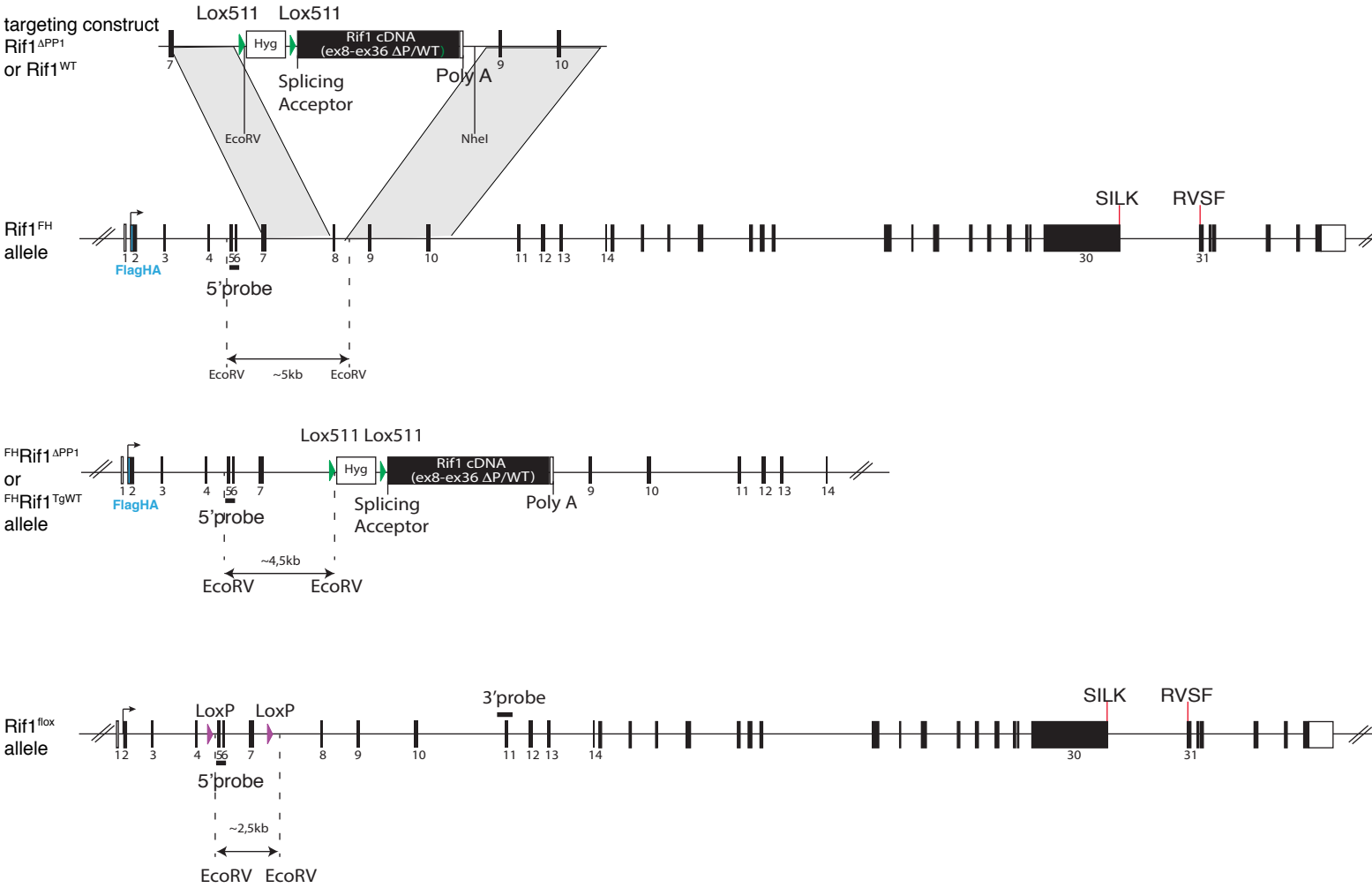

B

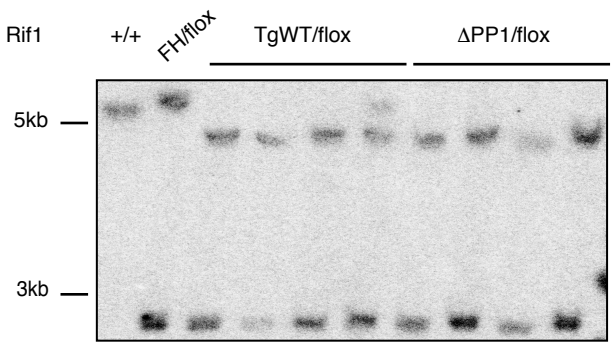

C

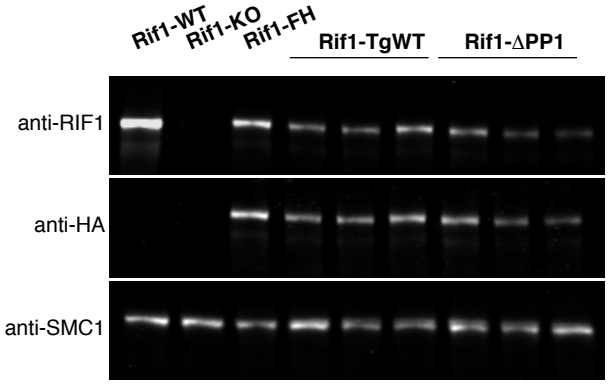

Figure S2

A

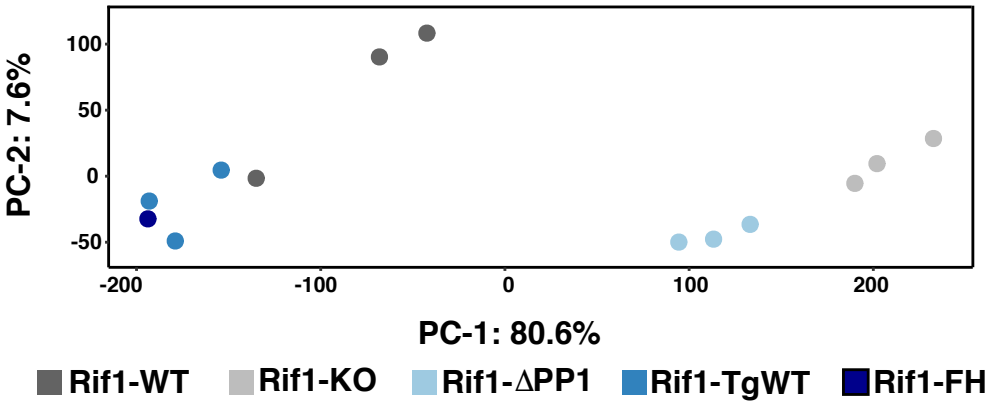

B

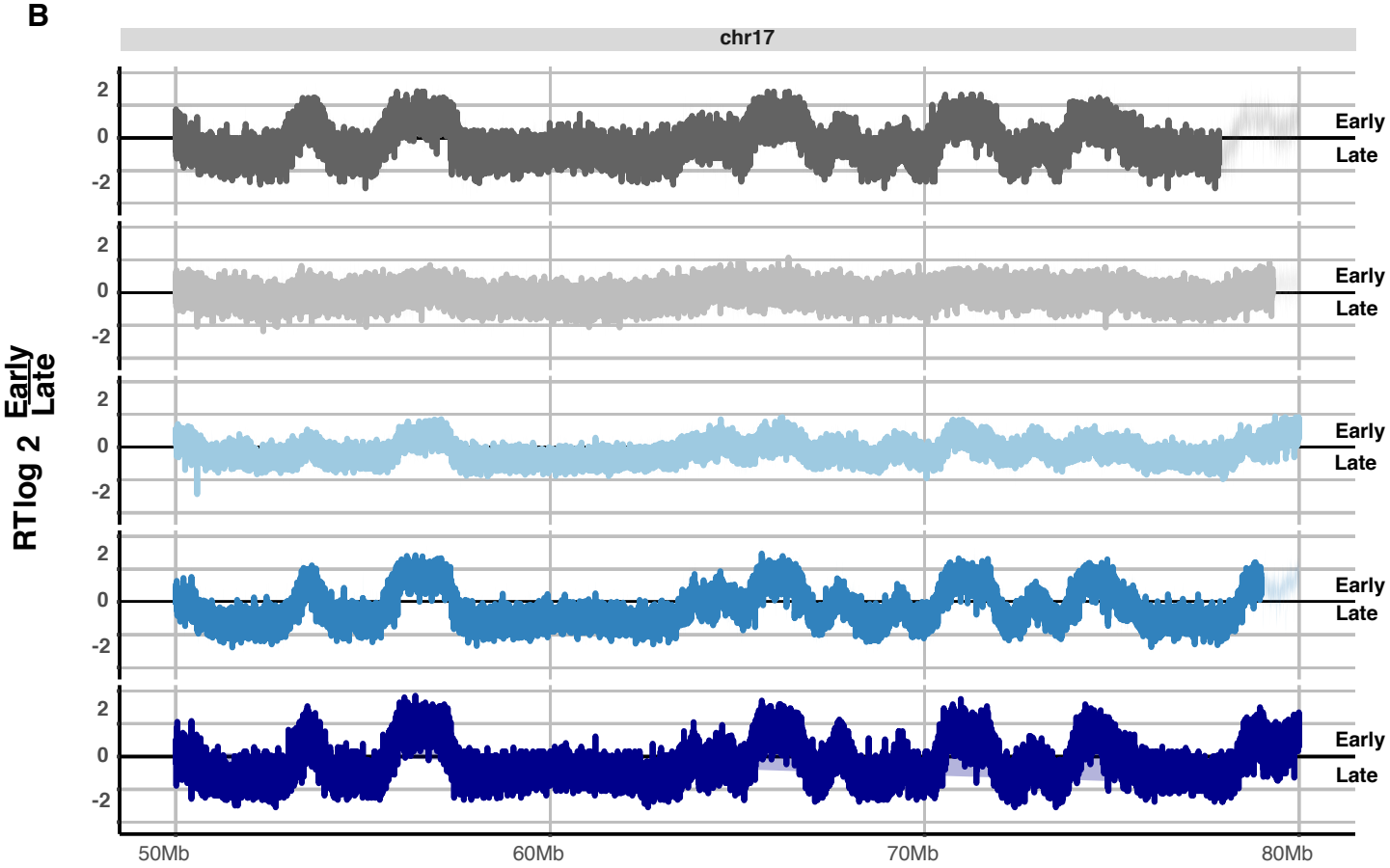

C

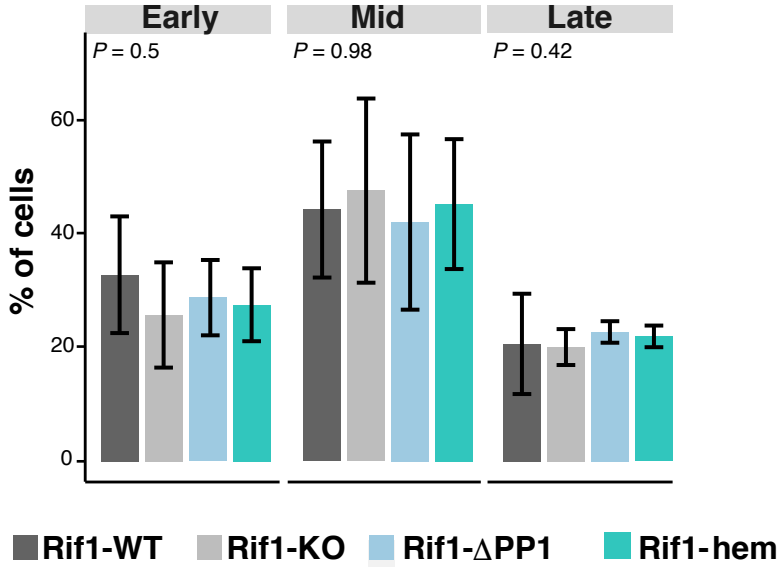

Figure S3

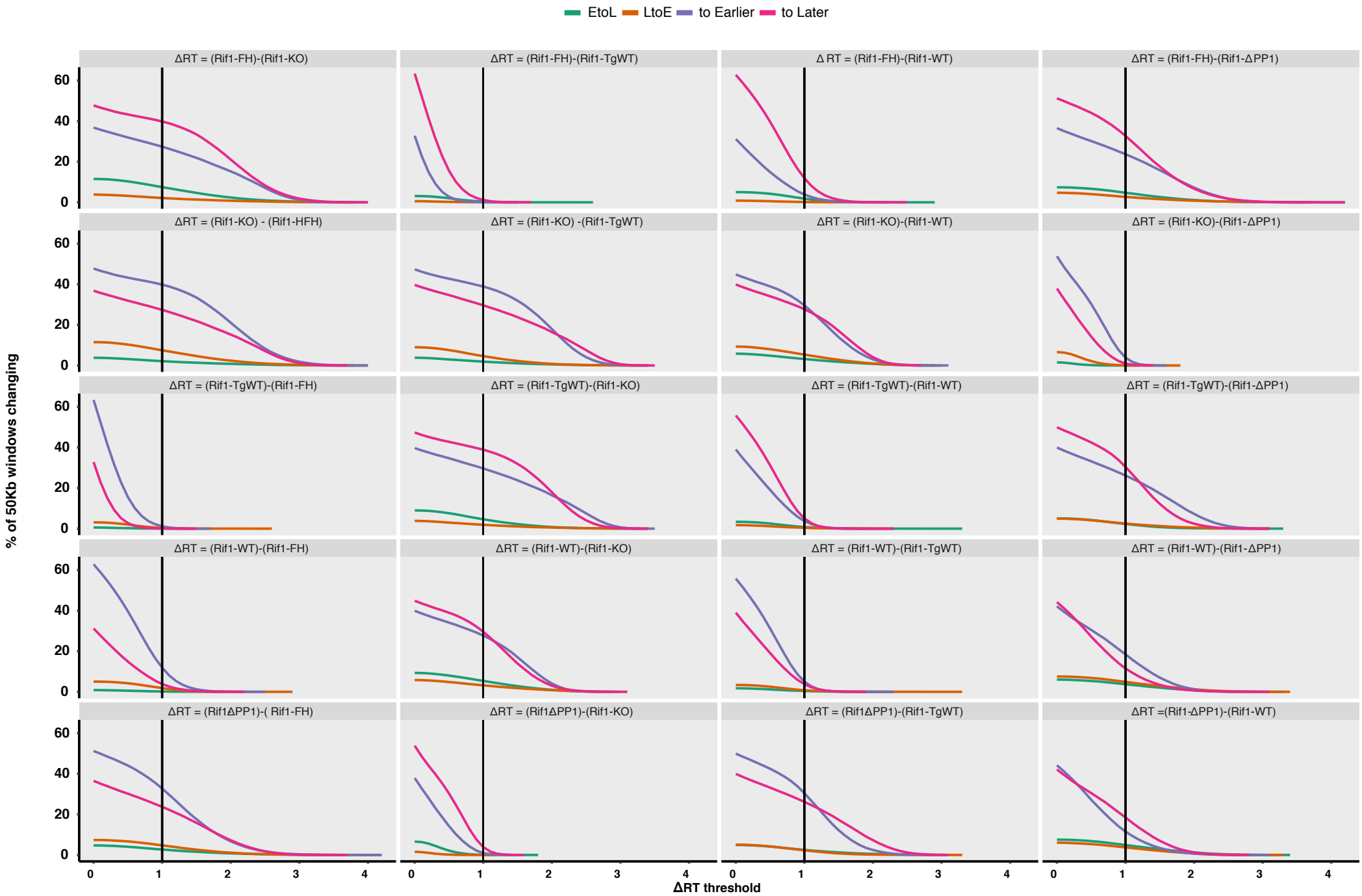
EtoL
LtoE
to Earlier
to Later
ΔRT = (Rif1-FH)-(Rif1-KO)
ΔRT = (Rif1-FH)-(Rif1-TgWT)
Δ RT = (Rif1-FH)-(Rif1-WT)
ΔRT = (Rif1-FH)-(Rif1-ΔPP1)
ΔRT = (Rif1-KO) - (Rif1-HFH)
ΔRT = (Rif1-KO) -(Rif1-TgWT)
ΔRT = (Rif1-KO)-(Rif1-WT)
ΔRT = (Rif1-KO)-(Rif1-ΔPP1)
ΔRT = (Rif1-TgWT)-(Rif1-FH)
ΔRT = (Rif1-TgWT)-(Rif1-KO)
ΔRT = (Rif1-TgWT)-(Rif1-WT)
ΔRT = (Rif1-TgWT)-(Rif1-ΔPP1)
ΔRT = (Rif1-WT)-(Rif1-FH)
ΔRT = (Rif1-WT)-(Rif1-KO)
ΔRT = (Rif1-WT)-(Rif1-TgWT)
ΔRT = (Rif1-WT)-(Rif1-ΔPP1)
ΔRT = (Rif1ΔPP1)-(Rif1-FH)
ΔRT = (Rif1ΔPP1)-(Rif1-KO)
ΔRT = (Rif1ΔPP1)-(Rif1-TgWT)
ΔRT =(Rif1-ΔPP1)-(Rif1-WT)
% of 50Kb windows changing
0
20
40
60
0
1
2
3
4
ΔRT threshold

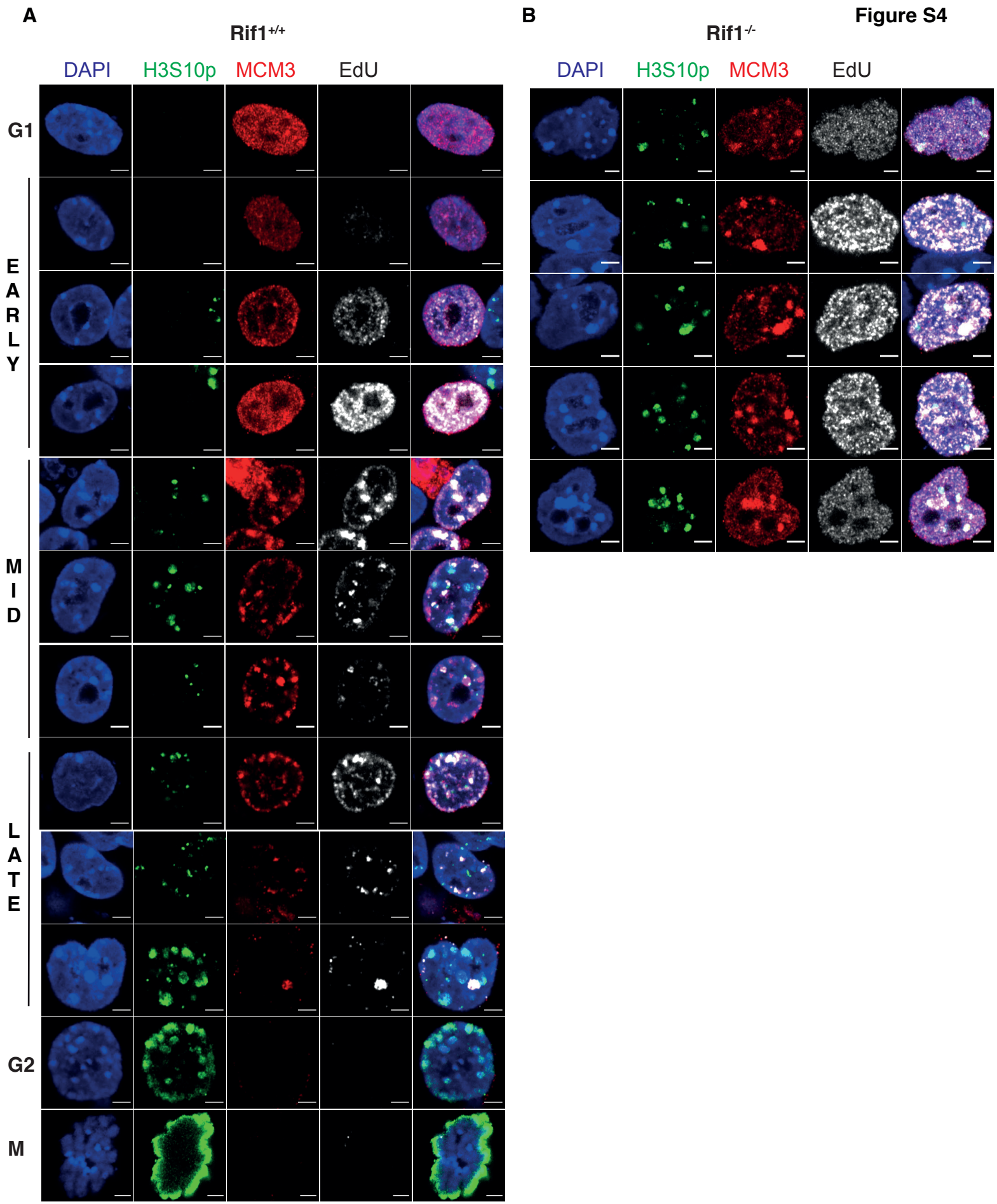
A
Rif1+/+
DAPI
H3S10p
MCM3
EdU
G1
EARLY
MID
LATE
G2
M
B
Rif1-/-
DAPI
H3S10p
MCM3
EdU

Figure S4

Figure S5

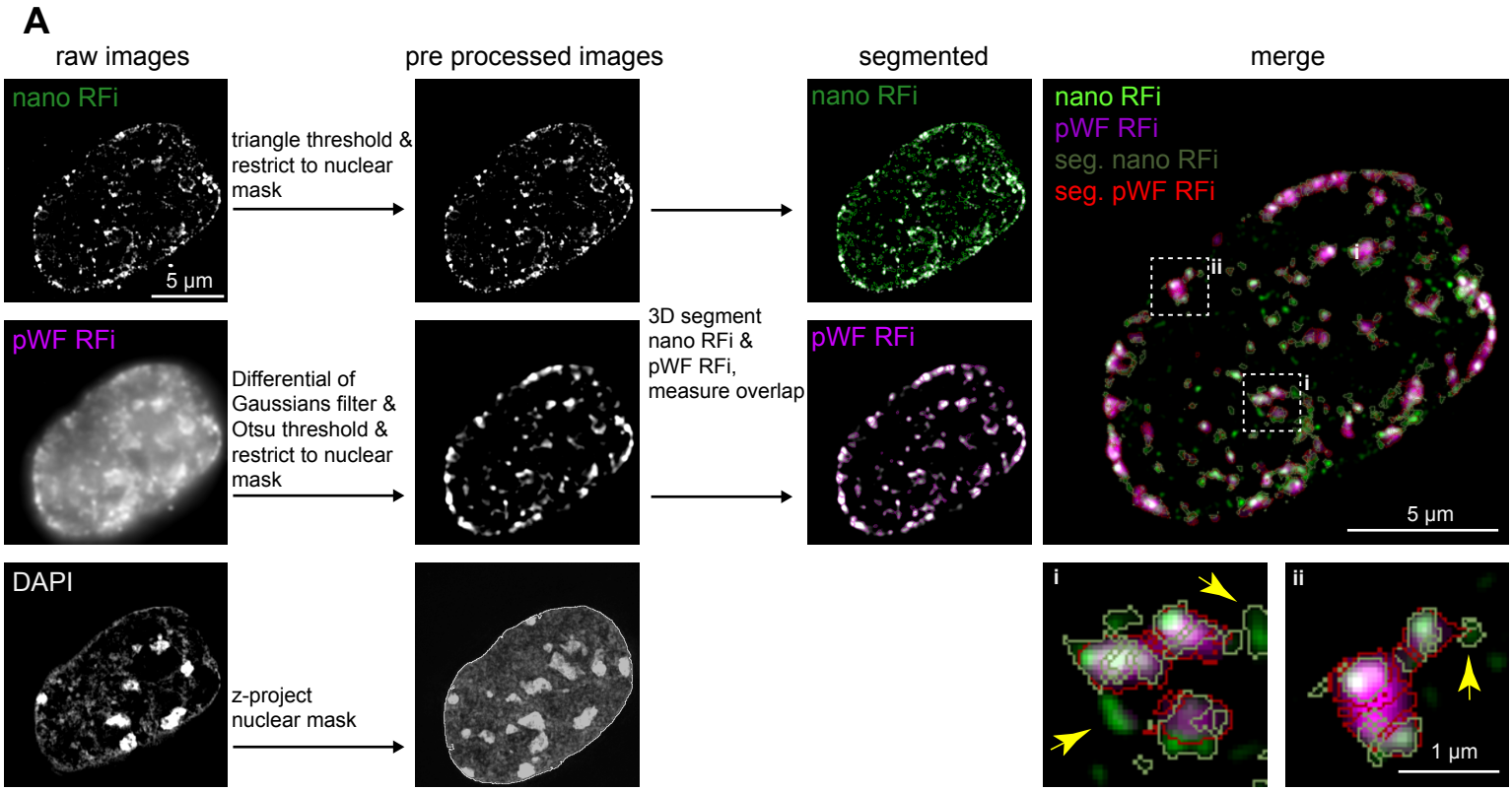
A
raw images
pre processed images
segmented
merge
nano RFi
5 µm
triangle threshold & restrict to nuclear mask
pWF RFi
Differential of Gaussians filter & Otsu threshold & restrict to nuclear mask
DAPI
z-project nuclear mask
3D segment nano RFi & pWF RFi, measure overlap
nano RFi
pWF RFi
nano RFi
pWF RFi
seg. nano RFi
seg. pWF RFi
ii
i
5 µm
i
ii
1 µm

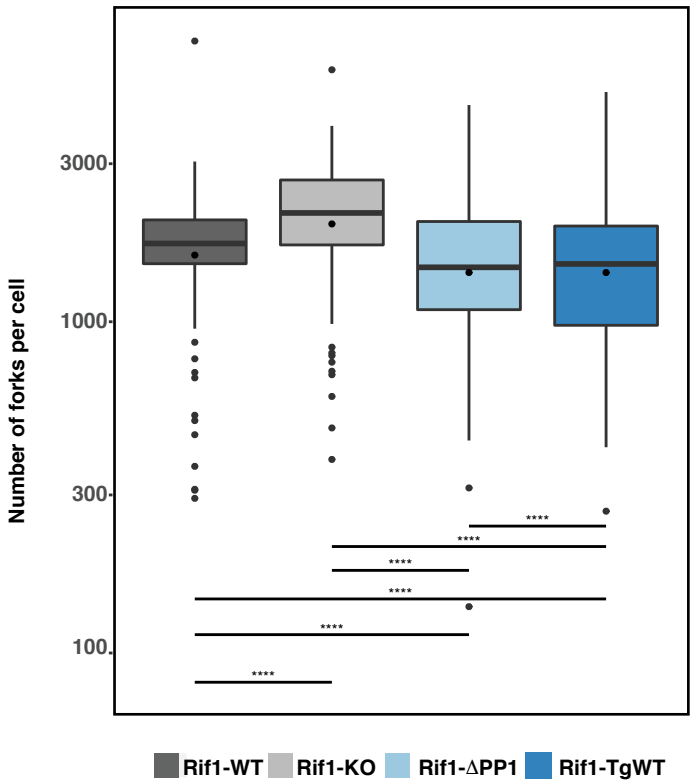
B
Number of forks per cell
3000
1000
300
100
****
Rif1-WT
Rif1-KO
Rif1-ΔPP1
Rif1-TgWT

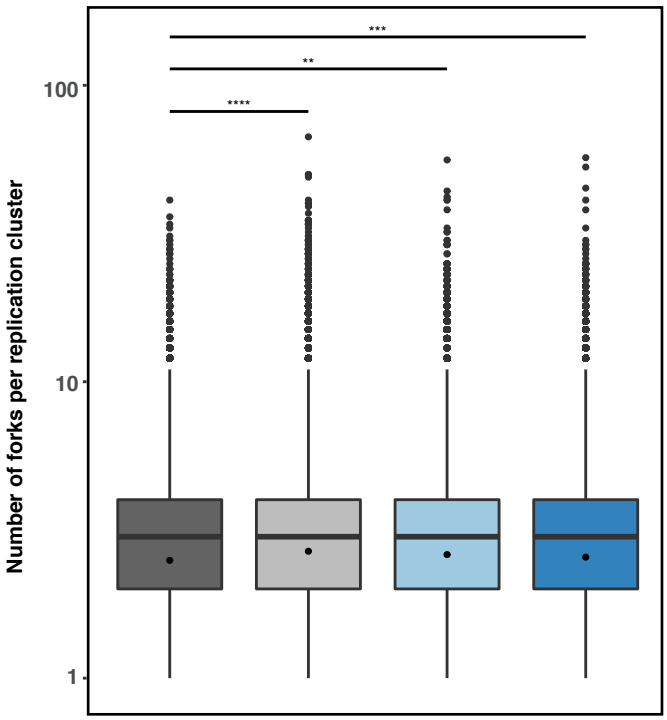
C
Number of forks per replication cluster
100
10
1
***
**
****